The Astrophysical Journal, 839:110 (23pp), 2017 April 20 https://doi.org/10.3847/1538-4357/aa67e8

Living on a Flare: Relativistic Reflection in V404 Cyg Observed by *NuSTAR* during Its Summer 2015 Outburst

D. J. Walton[1,2,3], K. Mooley[4], A. L. King[5], J. A. Tomsick[6], J. M. Miller[7], T. Dauser[8], J. A. García[2,8,9], M. Bachetti[10], M. Brightman[2], A. C. Fabian[3], K. Forster[2], F. Fürst[2], P. Gandhi[11], B. W. Grefenstette[2], F. A. Harrison[2], K. K. Madsen[2], D. L. Meier[1,2], M. J. Middleton[11], L. Natalucci[12], F. Rahoui[13,14], V. Rana[2], and D. Stern[1]

[1] Jet Propulsion Laboratory, California Institute of Technology, Pasadena, CA 91109, USA
[2] Space Radiation Laboratory, California Institute of Technology, Pasadena, CA 91125, USA
[3] Institute of Astronomy, University of Cambridge, Madingley Road, Cambridge CB3 0HA, UK
[4] Department of Physics, Oxford University, Denys Wilkinson Building, Keble Road, Oxford OX1 3RH, UK
[5] Einstein Fellow, Department of Physics, Stanford University, 382 Via Pueblo Mall, Stanford, CA 94305, USA
[6] Space Sciences Laboratory, University of California, Berkeley, CA 94720, USA
[7] Department of Astronomy, University of Michigan, 1085 S. University Avenue, Ann Arbor, MI, 49109-1107, USA
[8] ECAP-Erlangen Centre for Astroparticle Physics, Sternwartstrasse 7, D-96049 Bamberg, Germany
[9] Harvard-Smithsonian Center for Astrophysics, 60 Garden Street, Cambridge, MA 02138, USA
[10] INAF/Osservatorio Astronomico di Cagliari, via della Scienza 5, I-09047 Selargius (CA), Italy
[11] Department of Physics and Astronomy, University of Southampton, Highfield, Southampton SO17 1BJ, UK
[12] Istituto di Astrofisica e Planetologia Spaziali, INAF, Via Fosso del Cavaliere 100, I-00133 Roma, Italy
[13] European Southern Observatory, K. Schwarzschild-Str. 2, D-85748 Garching bei Munchen, Germany
[14] Department of Astronomy, Harvard University, 60 Garden Street, Cambridge, MA 02138, USA

Received 2016 September 2; revised 2017 March 6; accepted 2017 March 17; published 2017 April 21

Abstract

We present first results from a series of *NuSTAR* observations of the black hole X-ray binary V404 Cyg obtained during its summer 2015 outburst, primarily focusing on observations during the height of this outburst activity. The *NuSTAR* data show extreme variability in both the flux and spectral properties of the source. This is partly driven by strong and variable line-of-sight absorption, similar to previous outbursts. The latter stages of this observation are dominated by strong flares, reaching luminosities close to Eddington. During these flares, the central source appears to be relatively unobscured and the data show clear evidence for a strong contribution from relativistic reflection, providing a means to probe the geometry of the innermost accretion flow. Based on the flare properties, analogies with other Galactic black hole binaries, and also the simultaneous onset of radio activity, we argue that this intense X-ray flaring is related to transient jet activity during which the ejected plasma is the primary source of illumination for the accretion disk. If this is the case, then our reflection modeling implies that these jets are launched in close proximity to the black hole (as close as a few gravitational radii), consistent with expectations for jet launching models that tap either the spin of the central black hole, or the very innermost accretion disk. Our analysis also allows us to place the first constraints on the black hole spin for this source, which we find to be $a^* > 0.92$ (99% statistical uncertainty, based on an idealized lamp-post geometry).

Key words: black hole physics – X-rays: binaries – X-rays: individual (V404 Cyg)

1. Introduction

V404 Cygni (hereafter, V404 Cyg, also known as GS 2023+338) is a well-known, dynamically confirmed black hole X-ray binary (BHB). The black hole, of mass 9–15 $M_{\odot}$, is in a 6.5d binary system with a lower mass K-type stellar companion, from which it accretes via Roche-lobe overflow (Casares et al. 1992; Wagner et al. 1992; Shahbaz et al. 1994; Sanwal et al. 1996; Khargharia et al. 2010). Located only 2.39 ± 0.14 kpc away (Miller-Jones et al. 2009), V404 Cyg is one of the closest black hole systems known (Corral-Santana et al. 2016; Tetarenko et al. 2016).

As a low-mass X-ray binary (LMXB), V404 Cyg spends the majority of its time in quiescence, and has become one of the key targets for studying black holes in this regime (e.g., Bernardini & Cackett 2014; Reynolds et al. 2014a; Rana et al. 2016). However, as with other LMXBs, it undergoes intense accretion outbursts, likely related to the hydrogen ionization instability (see Lasota 2001 for a review). Although these events are rare, during these outbursts, V404 Cyg becomes one of the brightest X-ray sources in the sky. The X-ray band is vital for studying the accretion flow. For BHBs, the thermal emission from the accretion disk, the high-energy power-law continuum (likely resulting from Compton up-scattering of the disk emission), and the disk reflection spectrum (resulting from irradiation of the disk) all contribute to the broadband X-ray emission (e.g., Zdziarski et al. 2002; Reis et al. 2010; Walton et al. 2012; Tomsick et al. 2014; see Done et al. 2007 for a review). The disk reflection spectrum is particularly critical because this carries information regarding both the geometry of the innermost accretion flow (e.g., Wilkins & Fabian 2012; Dauser et al. 2013) and the spin of the central black hole (e.g., Miller et al. 2009; Reis et al. 2009; Brenneman et al. 2011; Walton et al. 2013; see Reynolds 2014 and Middleton 2015 for recent reviews). V404 Cyg is therefore an important source with which to investigate these accretion phenomena.

However, in some respects, V404 Cyg is unusual for a black hole LMXB. Throughout a typical outburst, most sources follow a relatively well-defined pattern of accretion states (see Fender & Gallo 2014; Belloni & Motta 2016 for recent reviews). Sources rise from quiescence into the hard state, in which the power law dominates the emission and persistent radio jets are seen. As the accretion rate continues to increase, sources transition into the soft state, in which the thermal

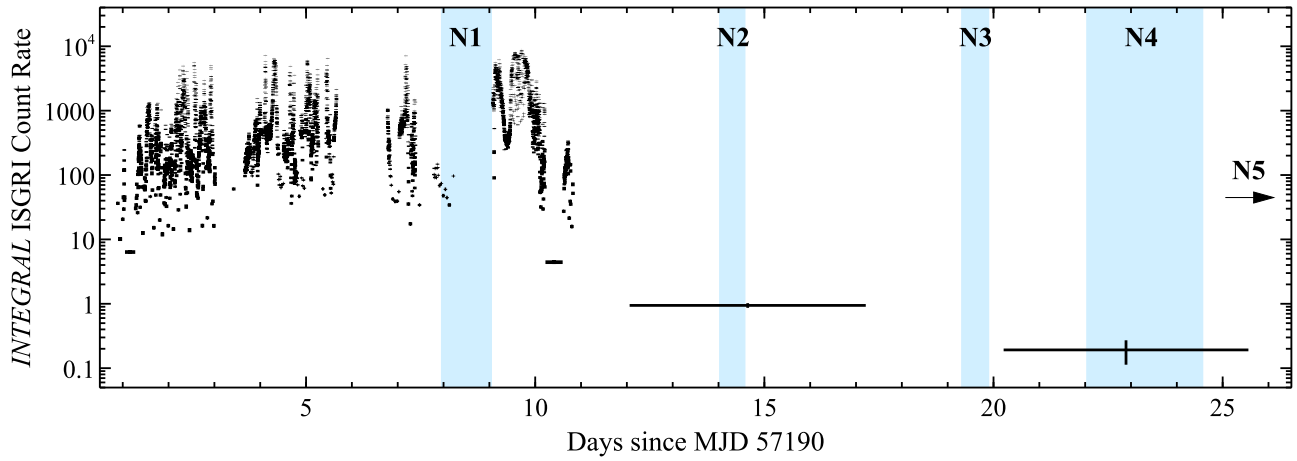

Figure 1. Long-term 25–200 keV X-ray light curve for the recent outburst from V404 Cyg observed with *INTEGRAL* (see Kuulkers & Ferrigno 2016 for details). The first four of our five *NuSTAR* observations are indicated with the shaded regions (N1–4; the fifth, N5, spanned MJD ∼57226.35–57227.46); the first caught V404 Cyg during the height of its activity, and is the subject of this work, while the following four observations probed various stages of its decline back to quiescence (V. Rana et al. 2017, in preparation).

emission from the disk dominates the observed emission. The radio jets are believed to be quenched in this state, and outflows are typically seen in the form of winds from the accretion disk instead (e.g., Miller et al. 2006; Neilsen & Lee 2009; Ponti et al. 2012, though recent analyses suggest that jets and disk winds may not necessarily be mutually exclusive, Rahoui et al. 2014; Reynolds et al. 2015; Homan et al. 2016). Then, as the sources fade, they move back through the hard state, before finally returning to quiescence.

V404 Cyg instead shows much more complexity. Its major 1989 outburst, which first identified the source as an X-ray binary, was well covered by the *Ginga* observatory (Kitamoto et al. 1989; Terada et al. 1994; Oosterbroek et al. 1997; Zycki et al. 1999a, 1999b). These observations revealed extreme levels of variability across a wide range of timescales. In part, this was driven by large variations in the line-of-sight absorption column, which was often significantly in excess of that seen during quiescence. Such variations are not typically seen in other black hole LMXBs. This strong and variable absorption resulted in complex X-ray spectra, making the identification of standard accretion states extremely challenging. In addition, evidence for X-ray reprocessing from both ionized and neutral material was observed at varying intervals, further complicating spectral decomposition (e.g., Zycki et al. 1999a).

In the summer of 2015, V404 Cyg underwent its first major outburst since 1989, triggering an enormous multi-wavelength observing campaign (e.g., King et al. 2015; Natalucci et al. 2015; Rodriguez et al. 2015; Roques et al. 2015; Gandhi et al. 2016; Jenke et al. 2016; Kimura et al. 2016; Motta et al. 2016; Muñoz-Darias et al. 2016, as well as many other works in preparation). As part of this broadband follow-up effort, we undertook a series of high-energy X-ray observations with the *Nuclear Spectroscopic Telescope Array* (*NuSTAR*; Harrison et al. 2013). Its unique combination of unprecedented high-energy sensitivity and broad bandpass (3–79 keV) make *NuSTAR* extremely well suited for disentangling the contributions from reflection and absorption (as demonstrated, for example, by the recent broadband work on the active galaxy NGC 1365; Risaliti et al. 2013; Walton et al. 2014; Kara et al. 2015; Rivers et al. 2015), and allows detailed, broadband spectroscopy to be performed on timescales much shorter than previously accessible. Critically for V404 Cyg, *NuSTAR*'s triggered read-out means it is also well suited to observing sources with extremely high count rates (e.g., Miller et al. 2013; Fürst et al. 2015; Parker et al. 2016; Walton et al. 2016), providing clean, high signal-to-noise measurements of their spectra without suffering from instrumental issues like photon pile-up, etc.

In this work, we present results from our 2015 *NuSTAR* campaign on V404 Cyg, focusing on observations made at the height of the outburst activity. The paper is structured as follows: Section 2 describes the *NuSTAR* observations and our data reduction procedure, Sections 3 and 4 present our analysis of the temporal and spectral variability exhibited by V404 Cyg, and Section 5 presents a discussion of the results obtained. Finally, we summarize our main conclusions in Section 6.

2. Observations and Data Reduction

Triggered by the summer 2015 outburst, we undertook five observations with *NuSTAR*. The timing of these observations is shown in the context of the long-term variability seen by *INTEGRAL* in Figure 1; the first was undertaken during the height of the activity from the source, and the remaining four were spaced throughout the following few weeks (Walton et al. 2015a, 2015b), during which V404 Cyg declined back to quiescence (Sivakoff et al. 2015a, 2015b). In this work, we focus on the first observation. Although this is split over two OBSIDs (90102007002, 90102007003), in reality, they comprise one continuous observation. The subsequent *NuSTAR* observations will be presented in V. Rana et al. (2017, in preparation).

The *NuSTAR* data were reduced, largely following standard procedures. Unfiltered event files were cleaned using NUPIPELINE, part of the *NuSTAR* Data Analysis Software (v1.5.1; part of the standard HEASOFT distribution), and instrumental responses from *NuSTAR* CALDB v20150316 are used throughout this work. Due to the high count rate and rapid variability, it was necessary to turn off some of the filtering for hot pixels normally performed by NUPIPELINE, since source counts were being removed from the peak flares. We did this by setting the "statusexpr" parameter to "b0000xx00xx0xx000," which controls the filtering on the STATUS column. In this way,

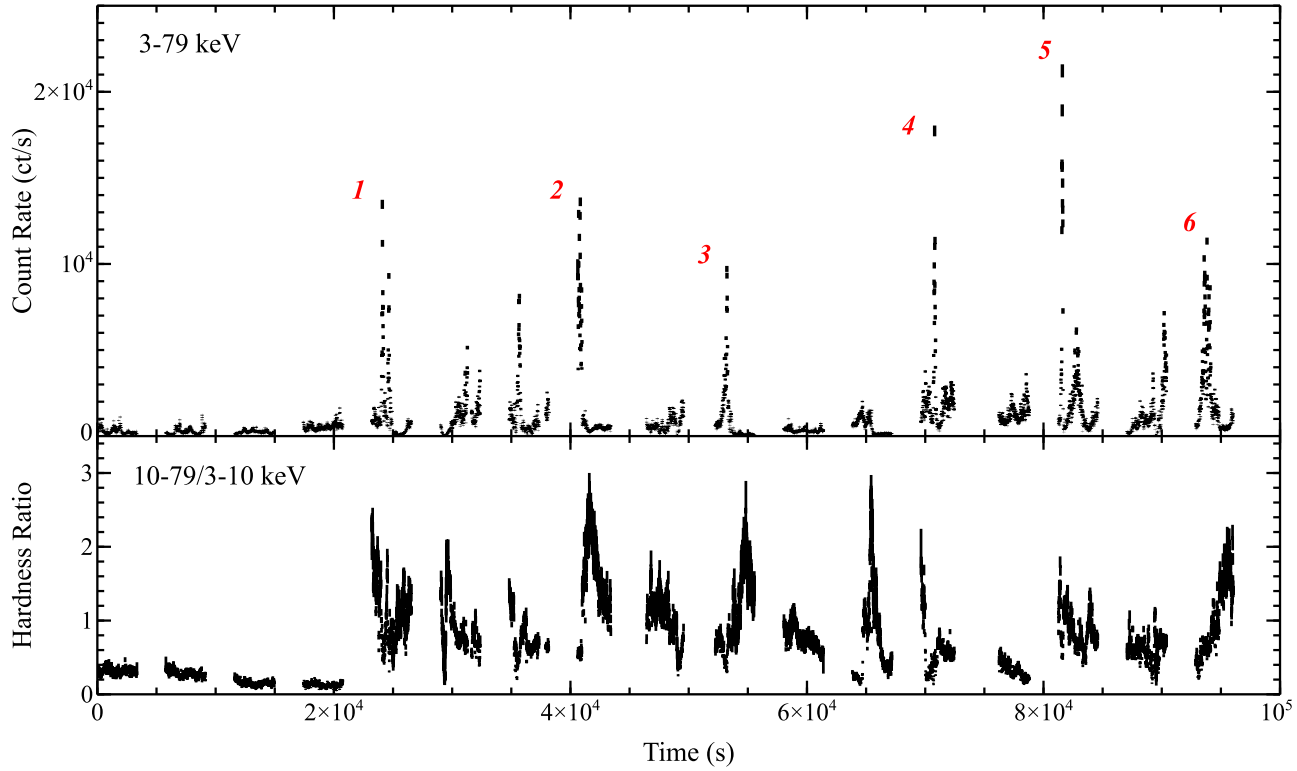

Figure 2. *NuSTAR* light curve for the first observation of V404 Cyg (top panel, 10 s bins). Only the FPMA data are shown for clarity, and the count rates have been corrected for the increasing deadtime that occurs at very high fluxes. For reference, the beginning of the observation corresponds to MJD 57197.935. After the first four *NuSTAR* orbits, extreme flaring is observed with incident count rates exceeding 10,000 ct s^{-1} on several occasions. The strongest six flares, analyzed in Section 4.3, are highlighted (red numbers). We also show the evolution of a broadband hardness ratio, computed between 3–10 and 10–79 keV (bottom panel). Strong spectral variability is observed throughout this latter flaring phase.

we kept the source events that were incorrectly identified as hot/flickering. The *NuSTAR* calibration database has a list of hot/flickering pixels that have already been identified, which were still removed following standard procedures. Passages of *NuSTAR* through the South Atlantic Anomaly were also excluded from our analysis.

Source products were then extracted from the cleaned events from a circular region centered on the source (radius 160″) using NUPRODUCTS for both focal plane modules (FPMA and FPMB). V404 Cyg is easily detected across the whole 3–79 keV *NuSTAR* bandpass. Owing to its extreme brightness, there were no regions of the detector on which V404 Cyg was located that were free of source counts, so the background was estimated from a blank region on the detector furthest from the source position (each FPM contains four detectors in a 2×2 array) in order to minimize any contribution from the source to our background estimation. Although there are known to be variations in the background between the detectors for each FPM, these differences are typically only at the 10% level (in the background rate) at the highest energies of the *NuSTAR* bandpass (where the internal detector background dominates; Wik et al. 2014). V404 Cyg is always a factor of >10 above the estimated background at all energies in the spectra extracted here, so such effects are negligible. Finally, when necessary, data from the two OBSIDs were combined using ADDASCAS-PEC for each FPM (though, we do not combine the FPMA and FPMB data), and all spectra were grouped such that each spectral bin contains at least 50 counts per energy bin, to allow the use of χ^2 minimization during spectral fitting.

3. Temporal Variability

In Figure 2 (top panel), we show the light curve observed by *NuSTAR*. The count rate shown is the incident count rate inferred rather than that directly recorded, i.e., the rate has been corrected for the deadtime (see Harrison et al. 2013; Bachetti et al. 2015). The most striking aspect is the strong flaring seen throughout the majority of the observation, during which the flux observed from V404 Cyg can rapidly increase by at least an order of magnitude. Many flares comfortably exceed rates of 10,000 ct s^{-1} (unless stated otherwise, count rates are quoted per FPM), with the most extreme even exceeding 20,000 ct s^{-1}. For reference, the incident 3–79 keV count rate for the Crab Nebula is ∼500 ct s^{-1} (Madsen et al. 2015b). Strong X-ray flaring from V404 Cyg has been reported by several authors throughout this outburst (e.g., King et al. 2015; Natalucci et al. 2015; Rodriguez et al. 2015; Roques et al. 2015; Jenke et al. 2016; Sanchez-Fernandez et al. 2016). We stress again that, even at these count rates, the *NuSTAR* data do not suffer significantly from pile-up; at similar count rates, Sco X-1 only had a pile-up fraction of ∼0.08% (see Appendix C in Grefenstette et al. 2016).

In addition to the extreme flux variability, we also see strong spectral variability throughout the *NuSTAR* observation. Figure 2 (bottom panel) shows the evolution of a simple broadband hardness ratio, computed as the ratio between the count rates in the 3–10 and 10–79 keV energy bands, which shows a remarkable transition between the fourth and fifth *NuSTAR* orbits. During the first four orbits, the hardness ratio is relatively stable, but after this point it becomes strongly variable. This transition is roughly coincident with the onset of

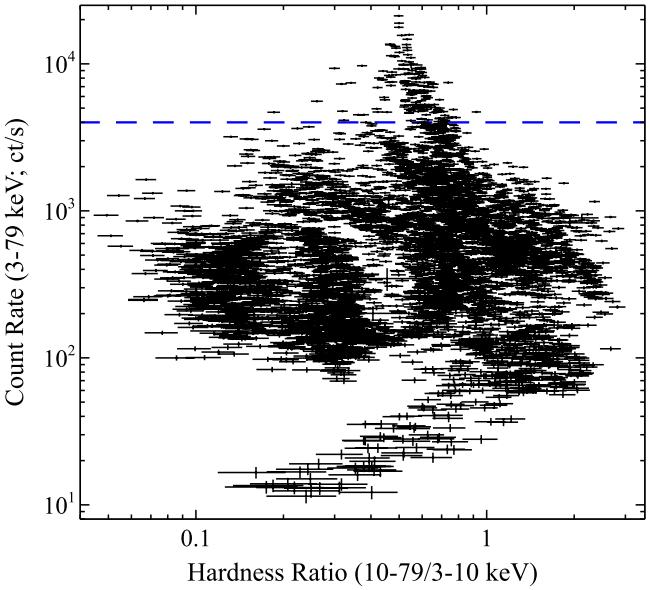

Figure 3. Hardness ratio–intensity diagram constructed from the data shown in Figure 2. The behavior seen during this *NuSTAR* observation is extremely complex. However, the strongest flares all show similar hardness ratios. The dashed blue line marks the count rate limit adopted in extracting the flare spectra discussed in Sections 4.1 and 4.3.

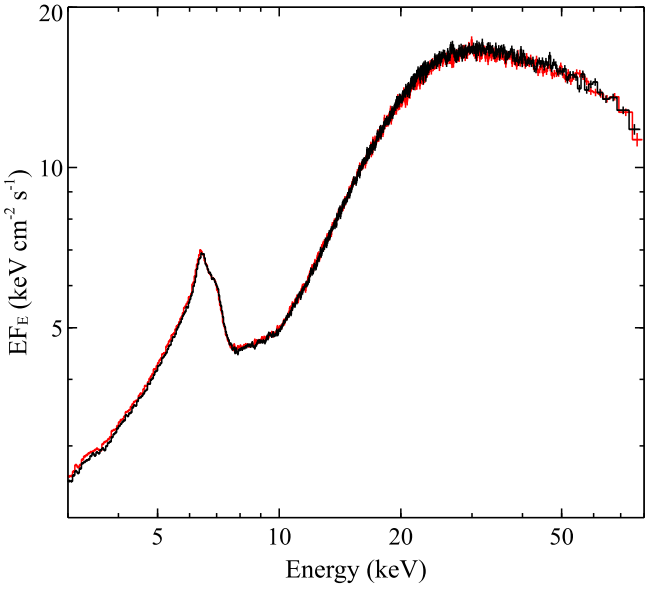

Figure 4. Average X-ray spectrum from our first *NuSTAR* observation of V404 Cyg. FPMA data are shown in black, and FPMB data are shown in red; both have been unfolded through a model that is constant with energy, and have been further rebinned for visual purposes. While strong spectral variability is observed throughout the observation, the average spectrum is still useful for highlighting certain features, noteably a narrow iron emission component, indicating the presence of reprocessing by distant material, and a strong absorption edge at ∼7 keV, indiciating the presence of absorption significantly in excess of the Galactic column throughout much of the observation.

the flaring portion of the observation. The data from the first four orbits will be discussed in more detail in a dedicated paper (D. J. Walton et al. 2017, in preparation); here we focus on the strong flaring seen throughout the majority of the *NuSTAR* observation.

In order to further characterize the observed variability, in Figure 3, we plot the 10–79/3–10 keV hardness ratio against the full 3–79 keV count rate. The resulting "hardness ratio–intensity" (HRI) diagram is rather chaotic, with no clear single trend and a lot of complex structure. There are two distinct "clouds" at moderate intensity with softer spectra (lower hardness ratio, $\lesssim$0.4), which primarily correspond to the data from the first four *NuSTAR* orbits. The more complex behavior seen in the rest of the data arises from the flaring period. Noteably, though, the flares themselves all appear to have similar hardness ratios. Finally, at the very lowest fluxes observed, there also appears to be a clear positive correlation between flux and hardness ratio, which breaks down above ∼100 ct s^{-1}.

4. Spectral Analysis

The majority of this work focuses on spectral analysis of data extracted from the period of intense flaring observed by *NuSTAR*. Our spectral analysis is performed with XSPEC v12.6.0f (Arnaud 1996), and parameter uncertainties are quoted at 90% confidence for one parameter of interest throughout this work (i.e., $\Delta\chi^2 = 2.71$). Residual cross-calibration flux uncertainties between the FPMA and FPMB detectors are accounted for by allowing multiplicative constants to float between them, fixing FPMA to unity; the FPMB constants are always found to be within 5% of unity, as expected (Madsen et al. 2015a).

In Figure 4, we show the average spectrum obtained from the full *NuSTAR* observation. Given the strong spectral variability discussed previously, a detailed analysis of this average spectrum would not be particularly meaningful. However, a visual inspection is still useful in terms of highlighting some of the features of the observed data. In particular, there is clear structure in the iron K bandpass. There is a strong absorption edge above 7 keV, indicating that there is absorption in excess of the Galactic column ($N_{\rm H,Gal} \sim 10^{22}$ cm^{-2}; e.g., Bernardini & Cackett 2014; Reynolds et al. 2014a; Rana et al. 2016) throughout much of the observation. This is similar to the 1989 outburst (e.g., Oosterbroek et al. 1997; Zycki et al. 1999a). In addition, as discussed by King et al. (2015) and Motta et al. (2016), there is a clear, narrow emission line from neutral iron, indicating a contribution from reprocessing by distant, neutral material; evidence for such emission was also seen in the 1989 data (Zycki et al. 1999a).

4.1. The Average Flare Spectrum

In Figure 5 (top panel), we show the average spectrum for the flares, extracted by selecting only periods where the count rate (per FPM) was >4000 ct s^{-1}. The total good exposure in the resulting spectrum is only ∼110–120 s. In contrast to the average spectrum, there is no visually apparent edge at ∼7 keV, indicating that the line-of-sight absorption is much weaker during these periods, and that we therefore have a cleaner view of the intrinsic spectrum. The flare spectrum is very hard, and there is still visible structure in the iron K band. In Figure 5 (bottom panel), we show the data/model residuals to a simple model consisting of a power-law continuum with a high-energy exponential cutoff, modified by a neutral absorption column, which is free to vary above a lower limit of 10^{22} cm^{-2} (set by prior constraints on the Galactic column; see above). We use the TBABS absorption model, adopting the ISM abundances

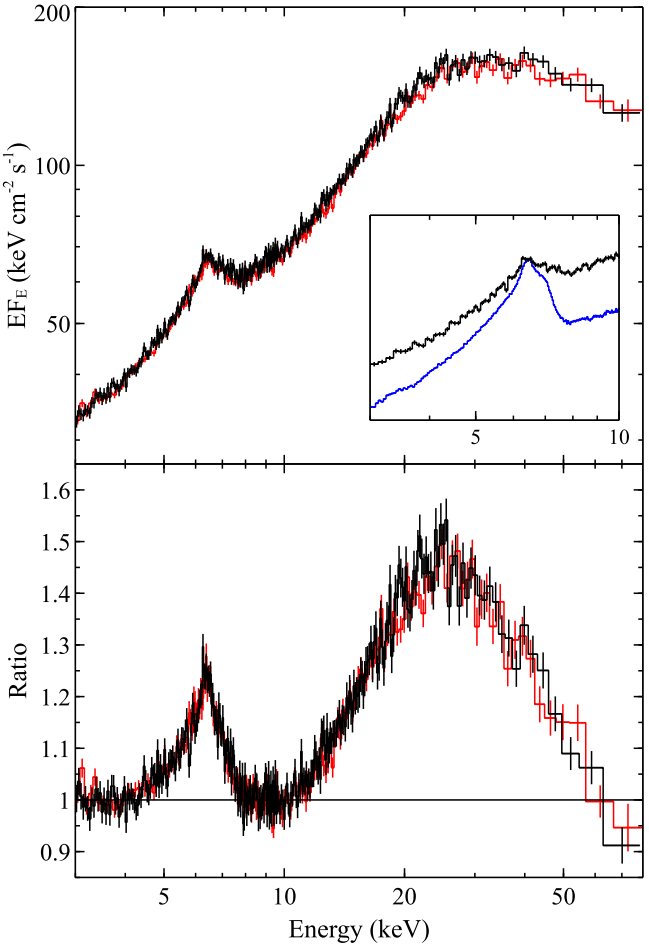

Figure 5. Flare spectrum, extracted from periods where the count rate (per FPM) exceeds 4000 ct s^{-1} (top panel, computed in the same manner as Figure 4). As before, the FPMA and FPMB data are shown in black and red, respectively, and the data have been further rebinned for visual purposes. The inset shows a comparison between the FPMA data for the flare spectrum and the average spectrum (blue) in the iron K bandpass, with the latter scaled up in flux so that the peaks of the narrow iron emission match; the strong edge seen in the average spectrum is not present in the flare spectrum. The bottom panel shows the data/model ratio to a simple power-law continuum with a high-energy exponential cutoff, fit to the 3–4, 8–10, and 50–79 keV bands. The residuals imply the presence of a strong reflection component from the inner accretion disk.

reported in Wilms et al. (2000) as our "solar" abundance set, and the cross-sections of Verner et al. (1996), as recommended. This model is fit to the 3–4, 8–10, and 50–79 keV energy ranges in order to minimize the influence of any reflected emission present in the spectrum. The photon index obtained is very hard, $\Gamma \sim 1.5$, with a cutoff energy of $E_{\rm cut} \sim 160$ keV.

A very strong Compton hump is visible around ~20–30 keV, indicating a significant contribution from X-ray reprocessing by optically thick material. The iron emission is also rather strong, and, although there is a narrow core to the line profile, the majority of the line emission is broadened with a clear red-wing, a hallmark of relativistically broadened reflection from an accretion disk (referred to as a "diskline" profile; e.g., Fabian et al. 1989; Laor 1991). Modeling the 3–10 keV bandpass with the simple continuum model above (fixing the cutoff energy to its best-fit value, given the limited energy range being considered), and including both an unresolved Gaussian at 6.4 keV and a RELLINE component

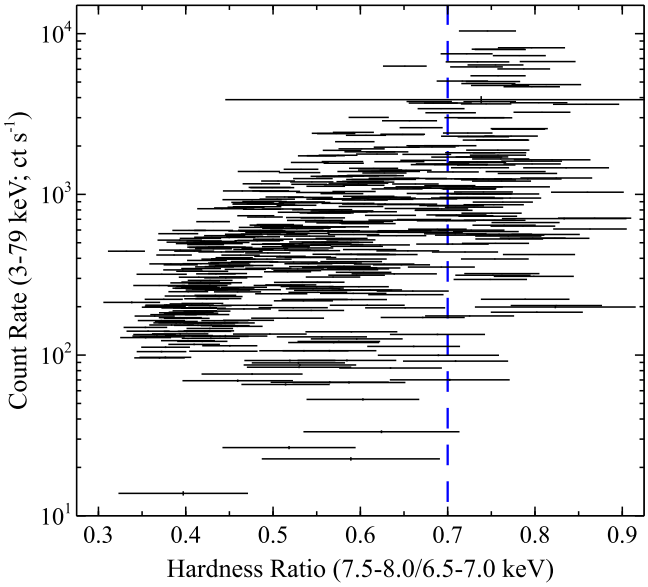

Figure 6. Hardness ratio–intensity diagram, similar to Figure 3 but with 100s time bins, for the narrow-band hardness ratio ($R_{\rm edge}$; see Section 4.2.1) constructed to probe the depth of the iron edge at ~7 keV. The major flares, which do not show the prominent edge seen in the average spectrum (Figures 4, 5), show $R_{\rm edge} > 0.7$ (indicated with the dashed blue line), which is used as a limit to identify other periods with similarly low levels of absorption.

(Dauser et al. 2010) to account for the narrow core and the iron emission from the accretion disk, respectively, we find that the RELLINE component has an equivalent width of EW ~ 400 eV, while the narrow core is much weaker, with EW ~ 25 eV.

4.2. Flux-resolved Spectral Evolution

Isolating and modeling the reprocessed emission from the accretion disk is of significant importance becuase this provides information on both the spin of the black hole (e.g., Risaliti et al. 2013; Walton et al. 2013, 2014; Reynolds 2014) and the geometry/location of the illuminating X-ray source (e.g., Wilkins & Fabian 2012). This is of particular interest for the intense flares, since such X-ray flares are often associated with jet ejection (e.g., Corbel et al. 2002). However, constraining the disk reflection is not necessarily straightforward from the iron band alone. In order to aid in disentangling the contributions from reprocessing by the accretion disk and by more distant material to the spectrum, the main body of this work focuses on modeling the broadband evolution of V404 Cyg as a function of flux during the flaring phase of our *NuSTAR* observation.

4.2.1. Data Selection

One of the main complications for broadband modeling is the strong and variable absorption that is present throughout this observation. In order to mimimize this issue, based on the flare spectrum (Figure 5), we select only periods of similarly low absorption for our flux-resolved spectral analysis. In order to identify such periods, we define a narrow-band hardness ratio (hereafter $R_{\rm edge}$), with the softer band (6.5–7.0 keV) just below the sharp edge seen in the average spectrum, and the harder band (7.5–8.0 keV) just above, such that we can track the strength of the edge throughout the flaring period. With

Table 1
Details of the Five Flux Bins Used in Our Flux-resolved Spectral Analysis of the Peruids of Low Absorption (Selected to Have $R_{\rm edge} \geqslant 0.7$)

Flux Bin	Count Rate (ct s^{-1} FPM^{-1})	Good Exposure (FPMA/B; s)	Broad Fe K EW (eV)
F1	100–500	1074/1105	260^{+70}_{-60}
F2	500–1000	1067/1120	350^{+60}_{-50}
F3	1000–2000	722/769	390^{+40}_{-80}
F4	2000–4000	260/280	460^{+60}_{-100}
F5	>4000	112/121	440^{+50}_{-90}

these narrow bands, a stronger absorption edge (and thus more absorption) would appear to have a softer spectrum (i.e., a lower hardness ratio). We show the behavior of $R_{\rm edge}$ in Figure 6, in the form of a similar HRI diagram to Figure 3. Note that we are forced to adopt a coarser temporal binning (100 s) in order for $R_{\rm edge}$ to be well constrained owing to the narrow energy bands used; hence the peak 3–79 keV count rates differ in this figure. Nevertheless, it is clear that in terms of $R_{\rm edge}$, the highest count rates (i.e., the strongest flares) show the hardest spectra, with $R_{\rm edge} \gtrsim 0.7$, consistent with the lack of absorption seen in Figure 5. Furthermore, though the majority of the observation shows a much stronger edge, there are other non-flare periods in which the absorption is similarly weak. These periods are spread randomly throughout the flaring portion of the observation, and span a broad range of flux.

We therefore select only data with $R_{\rm edge} \geqslant 0.7$ for the lower flux intervals (i.e., <4000 ct s^{-1}), and then divide these periods into four flux bins: 100–500, 500–1000, 1000–2000, and 2000–4000 ct s^{-1} (per FPM, using the count rates from the finer 10 s binning). The lower limit to the data considered is set to 100 ct s^{-1} in order to avoid the low flux region in which the flux and the broadband hardness ratio are correlated (see Figure 3), because the source behavior is clearly distinct in this regime. We therefore have five flux bins in total (referred to as F1–5, in order of increasing flux), including the flare spectrum extracted from >4000 ct s^{-1} in Section 4.1. Details of these flux bins are given in Table 1 and the extracted spectra are shown in Figure 7; the lack of strong, visible absorption edges in any of these spectra demonstrates the general success of our low-absorption selection procedure. As with the flare spectrum, despite the lack of strong absorption, the spectra from lower fluxes are also very hard. There are a couple of trends that can be seen from a visual inspection of these data. First, the relative contribution from the narrow core of the iron emission is stronger at lower fluxes. Second, the continuum above ~10 keV shows a lot more spectral curvature at higher fluxes.

Before proceeding with our more detailed spectral analysis, we repeat our phenomenological modeling of the 3–10 keV bandpass performed above for the flare spectrum, and fit the data for each of these flux bins with a combination of a broad and narrow iron emission component. In order to minimize parameter degeneracies, given the limited bandpass utilized, we make the simplifying assumption that the profile of the broad iron emission is the same for all fluxes. With this simple modeling, though the individual uncertainties are relatively large, we find that the strength of the broad iron emission increases with increasing flux (see Table 1).

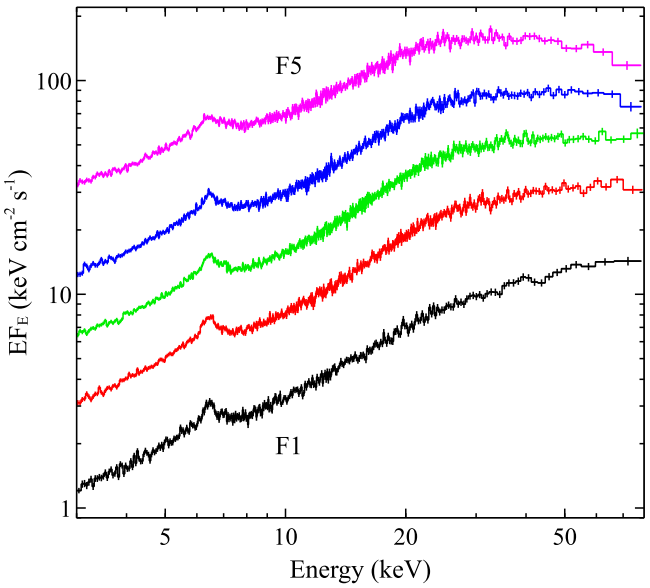

Figure 7. Five X-ray spectra extracted from periods of low absorption (determined based on the strength of the absorption edge at ~7 keV) for our flux-resolved analysis (F1–5, shown in black, red, green, blue, and magenta, respectively; the highest flux state, F5, is the same as the flare spectrum shown in Figure 5). Only the FPMA data are shown for clarity, and, as with Figures 4 and 5, the data have been unfolded through a constant, and the data have been rebinned for visual purposes. The X-ray spectrum visibly evolves with flux, with the continuum above ~10 keV becoming more peaked (i.e., there is more spectral curvature) at higher fluxes.

4.2.2. Basic Model Setup

Having extracted our low-absorption, flux-resolved *NuSTAR* data, we construct a spectral model for V404 Cyg that incorporates both the primary emission from the black hole, as well as X-ray reprocessing by both the accretion disk and more distant material. Our model also includes neutral absorption, allowing for both the Galactic column and a second absorption column, assumed to be intrinsic to the source, to account for any absorption in excess of the Galactic column.

To model the relativistic disk reflection, we use the RELXILL model (García et al. 2014). This is a merging of the XILLVER reflection model (v0.4c; García & Kallman 2010) with the RELCONV model for the relativistic effects close to a black hole that smear out the rest-frame reflection spectrum (Dauser et al. 2010). In particular, given the potential association between the X-ray flares and jet activity (as mentioned above, and discussed in more detail in Section 5.1), we use the RELXILLLP model (part of the broader RELXILL family of models). This includes both the primary continuum—assumed to be a power law with a high-energy exponential cutoff—and the reflected emission from the accretion disk, and treats the illuminating X-ray source as a point source located above the accretion disk on the spin-axis of the black hole (i.e., the "lamp-post" accretion geometry), an idealized geometrical approximation appropriate for the scenario in which the hard X-ray continuum is associated with the base of a jet (e.g., Markoff et al. 2005; Miller et al. 2012).

The key parameters for the RELXILLLP model are the photon index and the high-energy cutoff of the illuminating continuum (Γ, $E_{\rm cut}$), the spin of the black hole (a^*), the inclination and the inner and outer radii of the accretion disk

(i, $r_{\rm in}$, $r_{\rm out}$), the iron abundance and ionization parameter of the accreting material ($A_{\rm Fe}$, $\xi = 4\pi F/n$, where F is the ionizing flux incident on the disk, integrated between 1–1000 Ry, and n is the density of the material), the height of the illuminating source above the disk (h) and the strength of the disk reflection ($R_{\rm disk}$). Note that here, we use the "reflection fraction" definition outlined in Dauser et al. (2016). This determines the strength of the reflected emission from the relative intensities of the power-law continuum as seen by the disk and by the distant observer, which can be computed self-consistently for the lamp-post geometry via relativistic ray-tracing. The outer radius of the disk is set to 1000 $r_{\rm G}$ throughout our analysis (where $r_{\rm G}$ is the gravitational radius), the maximum permitted by the model, and following García et al. (2015), we consider cutoff energies up to 1000 keV. We also compute h in units of the event horizon ($r_{\rm H}$, which varies between 1 and 2 $r_{\rm G}$ for maximally rotating and non-rotating black holes, respectively) throughout this work, so that we can require that the X-ray source is always outside this radius. For practical reasons, we actually set a lower limit of 2 $r_{\rm H}$ for h in order to prevent the model from implying unphysically small X-ray sources, as the illuminating source obviously must have some physical extent (particularly if it is associated with a jet) despite being approximated in our models as a point source.

For the distant reprocessor, we use the XILLVER reflection model. Because the narrow core is at 6.4 keV, we assume this to be neutral (i.e., $\log \xi = 0$; throughout this work we quote ξ in units of erg cm s^{-1}). The key parameters here are the photon index and high-energy cutoff of the illuminating continuum, the inclination of the reflecting slab, the iron abundance, and the strength of the reflected emission. Both the photon index and the high-energy cutoff are assumed to be the same as for the RELXILLLP component, and as RELXILLLP already includes the primary continuum emission, we configure the XILLVER model to only provide the reflected emission (i.e., we set the reflection fraction parameter to -1). One complication is that the geometry of the distant reprocessor is not known, and different geometries can result in differences in the reflected spectra (e.g., Brightman et al. 2015). XILLVER assumes a simple semi-infinite slab, but this is unlikely to be physically realistic. Therefore, in order to allow the XILLVER component representing the distant reprocessor, the flexibility to differ from the simple slab approximation, we allow the iron abundance and inclination parameters of this component to vary independently of the other model components. These are effectively "dummy" parameters, which allow us to incorporate this flexibility with a simple parameterization. However, we set a lower limit on $A_{\rm Fe}$ of 0.9, such that the limit in which the distant reflection dominates the 2–10 keV bandpass would remain consistent with King et al. (2015), who report equivalent widths of up to 1 keV for the narrow, neutral iron emission based on their analysis of the high-resolution *Chandra* HETG data taken during this outburst.

King et al. (2015) also find both emission and absorption lines from Fe XXV and Fe XXVI. We therefore also allow for a contribution from photoionized emission and absorption. These are treated with grid models generated with XSTAR (Kallman & Bautista 2001), and are customized specifically for V404 Cyg. In brief, these grids are calculated assuming the abundances set derived by González-Hernández et al. (2011) for the stellar companion of V404 Cyg, and their free parameters are the ionization state of the material, its column density, and its outflow velocity (see A. L. King et al. 2017, in preparation, for full details). While King et al. (2015) find the absoption features to be mildly outflowing, the velocity shifts are small in comparison to the spectral resolution of *NuSTAR*, and we therefore keep these photoionized components fixed at rest.

Finally, for the neutral absorption, we again use the TBABS model. The Galactic column is set to $N_{\rm H,Gal} = 10^{22}$ $\rm cm^{-2}$, as discussed previously, and is assumed to have the ISM abundances of Wilms et al. (2000). For the additional, source intrinsic absorption, we use the version of TBABS with variable elemental abundances, so that we can link the iron abundance of this absorber to that of the disk reflection model (i.e., we assume that V404 Cyg is a chemically homogeneous system). We assume that this absorber is sufficiently distant from the innermost accretion flow that it should act on all of the emission components arising from this region. This absorber may potentially be associated with the distant reprocessor, and, to allow for this possibility, we configure the model such that while the Galactic absorption acts on all of the emission components, the source intrinsic absorber acts only on the primary emission and the relativistic disk reflection, but not the distant reflection. However, this choice makes little difference to the results obtained, because the distant reprocessor makes a negligible contribution to the spectrum at the lowest energies covered by *NuSTAR*. The form of the basic model applied, in XSPEC jargon, is therefore as follows: $\rm TBABS_{Gal} \times (XILLVER + XSTAR_{emis} + (XSTAR_{abs} \times TBABS_{src} \times RELXILLLP))$.

We apply this model to the five flux states shown in Figure 7 simultaneously. In doing so, we require the black hole spin, the inclination of the accretion disk, and the iron abundance of the system to be the same across all flux states, because these physical parameters should not vary over the course of this *NuSTAR* observation. Because it is unlikely that the geometry of the distant reprocessor would evolve significantly throughout our observation, we also link the "shape" parameters that would relate to geometry in our simple parameterization (iron abundance, slab inclination) for this component across all flux levels. However, we do allow this component to respond to the changes in the intrinsic emission from V404 Cyg. During the fitting process, we found that the ionizaion of the XSTAR absorption component was consistent for all of the flux states, so for simplicity we also linked this parameter. Additionally, we found that the photoionized emission only makes a significant contribution to the lowest flux state, F1, and thus we fixed its normalization to zero for F2–5. Furthermore, we found that this photoionized emission only provided an additional contribution to the narrow Fe K emission, and as such the column density and normalization were highly degenerate, so we fixed the former to an arbitrary value of 10^{19} $\rm cm^{-2}$.

4.2.3. Results

To begin with, we assume that the disk extends into the innermost stable circular orbit (ISCO) for all flux states and that the corona is not outflowing, and we allow the reflection fraction to vary as a free parameter (Model 1; a summary of all the models considered in our flux- and flare-resolved analyses is given in Table 2). This model provides a good fit to the global data set, with $\chi^2 = 10599$ for 10308 degrees of freedom (DoF). We observe several trends in the fits, which are presented in Table 3. Most notably, we find that the strength of

Table 2
A Summary of the Lamp-post Reflection Models Applied during Our Flux- and Flare-resolved Analyses, Presented in Sections 4.2 and 4.3, Respectively

Model	Data Set	Source Emission	Notes
1	Flux-resolved	Lamp-post only	$R_{\rm disk}$ a free parameter, $r_{\rm in}$ fixed at the ISCO
2	Flux-resolved	Lamp-post only	$R_{\rm disk}$ calculated self-consistently, $r_{\rm in}$ free to vary, h constant
3	Flux-resolved	Lamp-post only	$R_{\rm disk}$ calculated self-consistently, $r_{\rm in}$ fixed at the ISCO, h free to vary
4	Flux-resolved	Lamp-post + disk	$R_{\rm disk}$ calculated self-consistently, $r_{\rm in}$ free to vary, h constant
5	Flare-resolved	Lamp-post only	$R_{\rm disk}$ calculated self-consistently, $r_{\rm in}$ fixed at the ISCO
6	Flare-resolved	Lamp-post + disk	$R_{\rm disk}$ calculated self-consistently, $r_{\rm in}$ fixed at the ISCO
6i	Flare-resolved	Lamp-post + disk	Same as model 6, but i limited to $\geqslant 45^{\circ}$

Table 3
Results for the Free Parameters in the Basic Lamp-post Reflection Model (Model 1) Constructed for the Spectral Evolution As a Function of Flux

Model Component	Parameter		Global	Flux Level				
				F1	F2	F3	F4	F5
TBABS$_{\rm src}$	$N_{\rm H}$	(10^{21} cm^{-2})	...	$9.1^{+2.2}_{-1.7}$	$9.1^{+1.6}_{-2.1}$	<0.7	<1.6	<0.4
RELXILLLP	Γ	...	...	1.43 ± 0.02	1.49 ± 0.03	$1.42^{+0.02}_{-0.01}$	$1.41^{+0.02}_{-0.01}$	$1.40^{+0.01}_{-0.02}$
	$E_{\rm cut}$	(keV)	...	>840[a]	610^{+340}_{-210}	240^{+10}_{-20}	150^{+20}_{-10}	120 ± 10
	a^*	...	>-0.1	...	...	...	...	...
	i	($^{\circ}$)	27 ± 2	...	...	...	...	...
	h	($r_{\rm H}$)	...	$6.0^{+7.0}_{-2.0}$	$4.7^{+4.0}_{-1.0}$	$3.9^{+3.0}_{-1.1}$	$3.7^{+2.8}_{-0.9}$	$3.2^{+2.5}_{-1.1}$
	$\log \xi$	log (erg cm s^{-1})	...	$3.01^{+0.02}_{-0.01}$	3.02 ± 0.01	$3.09^{+0.01}_{-0.02}$	$3.15^{+0.05}_{-0.02}$	$3.47^{+0.05}_{-0.04}$
	$A_{\rm Fe}$	(solar)	$1.9^{+0.3}_{-0.1}$	...	...	...	...	...
	$R_{\rm disk}$	...	...	1.1 ± 0.2	$1.5^{+0.3}_{-0.2}$	$1.7^{+0.4}_{-0.2}$	$2.0^{+0.6}_{-0.2}$	$3.0^{+0.8}_{-0.5}$
	Norm	...	...	$0.15^{+0.03}_{-0.02}$	$0.23^{+0.05}_{-0.03}$	$0.33^{+0.08}_{-0.09}$	$0.47^{+0.09}_{-0.06}$	$0.65^{+0.34}_{-0.15}$
XSTAR $_{\rm abs}$	$\log \xi$	log (erg cm s^{-1})	$4.6^{+0.8}_{-0.3}$	...	...	...	...	...
	$N_{\rm H}$	(10^{21} cm^{-2})	...	$3.7^{+5.0}_{-2.3}$	$4.2^{+4.8}_{-1.5}$	<3.5	$3.4^{+4.0}_{-1.3}$	$3.0^{+2.7}_{-1.1}$
XILLVER	i[b]	($^{\circ}$)	<11	...	...	...	...	...
	$A_{\rm Fe}$[b]	(solar)	<0.91	...	...	...	...	...
	Norm	(10^{-2})	...	$1.2^{+1.1}_{-0.8}$	$8.6^{+0.7}_{-1.1}$	$12.7^{+0.8}_{-0.7}$	$18.7^{+1.6}_{-1.5}$	$33.0^{+2.7}_{-3.0}$
XSTAR $_{\rm emis}$	$\log \xi$	log (erg cm s^{-1})	...	<1.7	...	...	...	...
	Norm	(10^{4})	...	1.3 ± 0.3	...	...	...	...
χ^2/DoF			10599/10308					
F_{3-79}[c]	(10^{-8} erg cm^{-2} s^{-1})		...	3.78 ± 0.02	8.85 ± 0.03	16.06 ± 0.06	28.0 ± 0.1	54.6 ± 0.3

Notes.
[a] $E_{\rm cut}$ is constrained to be $\leqslant$1000 keV following García et al. (2015).
[b] These act as dummy "shape" parameters to allow this component the flexibility to deviate from the simple slab approximation adopted in the XILLVER model (see the main text), and in turn allow for our lack of knowledge with regards to the geometry of the distant reprocessor.
[c] Average flux in the 3–79 keV bandpass.

the disk reflection increases with increasing flux (see Figure 8). This is a strong indicator that the (average) geometry of the innermost accretion flow evolves as a function of source flux. In addition to these variations, the ionization of the disk increases as the observed flux increases, as would broadly be expected for an increasing ionizing flux, and there are changes in the intrinsic continuum, with the high-energy cutoff decreasing in energy as the flux increases.

The black hole spin is not well constrained with this model (though the majority of negative spins are excluded: $a^* > -0.1$). However, during the flares, the disk reflection is very strong, ($R_{\rm disk} \sim 3$). Caution over the exact value is necessary here, because the strength of the reflection obtained is dependent to some extent on the form of the high-energy curvature included in the input continuum model (a simple exponential cutoff in this work), and there is also some degeneracy between the $R_{\rm disk}$ and $E_{\rm cut}$ parameters. However, taking the result at face value, this would imply a scenario in which strong gravitational light bending enhances the disk reflection (e.g., Miniutti & Fabian 2004). In turn, this would imply that V404 Cyg hosts a rapidly rotating black hole (e.g., Dauser et al. 2014; Parker et al. 2014). Although we are using an idealized lamp-post geometry in this work, as long as the disk is thin, then this is the case regardless of the precise geometry of the X-ray source, because the disk must extend close to the black hole in order to subtend a sufficiently large solid angle to produce the high reflection fraction; the validity of the thin disk assumption (which is currently implicit in the RELXILL models) for these flares is discussed further in Section 5.2. Potential evidence for strong reflection during bright flares has also been seen from *INTEGRAL* observations of this outburst (Natalucci et al. 2015; Roques et al. 2015). We stress, though, that despite any degeneracy between these parameters, the variations in both $E_{\rm cut}$ and $R_{\rm disk}$ are significant;

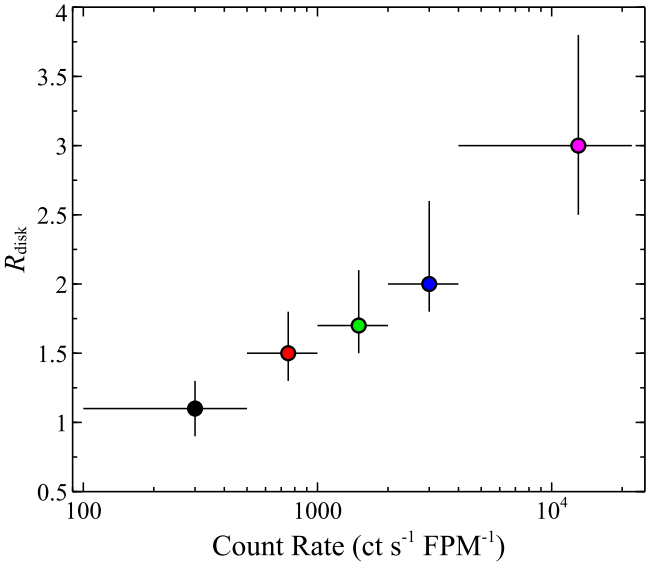

Figure 8. Evolution of the disk reflection fraction $R_{\rm disk}$ with source flux inferred from our basic lamp-post model for the spectral evolution seen from V404 Cyg (Model 1). We find that $R_{\rm disk}$ increases with increasing flux, implying an evolution in the geometry of the innermost accretion flow. The strong reflection found at the highest fluxes ($R_{\rm disk} \sim 3$) would require gravitational light bending. The data points are color-coded to match the spectra shown in Figure 7.

if we try to force one of these two parameters to be the same for each of the flux states and only allow the other to vary, the fits are significantly worse ($\Delta\chi^2 > 80$ for four fewer free parameters). While the absolute values themselves are somewhat model dependent, the trend of increasing $R_{\rm disk}$ with increasing flux appears to be robust to such issues.

For the disk reflection fraction to vary in such a manner, the solid angle subtended by the disk as seen by the X-ray source must decrease as the observed flux decreases. A few potential scenarios could produce such behavior: (1) the disk itself could evolve (e.g., truncate) such that it genuinely covers a smaller solid angle at lower fluxes; (2) the corona could evolve and vary its location/size, such that the degree of gravitational light bending is reduced; (3) the corona could alternately vary its velocity, such that the beaming away from the disk is increased. While some combination of these three effects is of course possible, and probably even likely should the flares be related to jet ejection events, from a practical standpoint their individual effects on the observed reflection emission are rather similar (Dauser et al. 2013; Fabian et al. 2014). Therefore, in order to investigate the potential geometric evolution without introducing further parameter degeneracies, we also modify our basic model to consider two limiting scenarios representing the first two of these three possibilities (Models 2 and 3, respectively), now making use of the fact that given a combination of black hole spin, inner disk radius, and X-ray source height, RELXILLLP can self-consistently compute the expected $R_{\rm disk}$ from the lamp-post geometry.[15] First, we assume that the corona remains static and the disk progressively truncates as the flux decreases, and second, we assume that the disk remains static and the corona progressively moves away from the disk (note that this could relate to either a physical movement of the corona, or a vertical expansion of the electron cloud).

In the truncation scenario (which we call Model 2), we therefore allow the inner radius of the disk ($r_{\rm in}$) to vary, though given the results above, we assume that during the flares the disk does reach the ISCO, and we link h across all flux states. For the lower flux states, $r_{\rm in}$ is computed in units of $r_{\rm ISCO}$, so that we can ensure that $r_{\rm in} \geqslant r_{\rm ISCO}$, as simulations find that emission from within the ISCO is negligible (e.g., Reynolds & Fabian 2008; Shafee et al. 2008). In the dynamic corona scenario (Model 3), we assume that the disk reaches the ISCO for all fluxes, and instead vary h. The results from these two scenarios are presented in Table 4; we focus only on the key RELXILLLP parameters because the parameters for the other components generally remain similar to Model 1.

Both of these scenarios provide reasonable fits to the data ($\chi^2/{\rm DoF} = 10656/10313$ and $10675/10312$ for Models 2 and 3, respectively), though the truncation scenario formally provides the better fit, and both are worse fits than Model 1 (in which $R_{\rm disk}$ is a free parameter), owing to the additional physical constraints imposed. With these additional constraints, both scenarios require the spin to be at least moderate ($a^* \gtrsim 0.6$), but above this value the χ^2 landscape becomes complex. Both scenarios show distinct minima that provide similarly good fits (different by $\Delta\chi^2 < 5$ in both cases) at a high spin value and at a more moderate-spin value (see Figure 9). For the truncating disk scenario (Model 2) the high spin solution ($a^* \sim 0.97$) is marginally preferred over the lower spin solution ($a^* \sim 0.82$), while for the dynamic corona scenario (Model 3) the lower spin solution ($a^* \sim 0.65$) is marginally preferred over the high spin solution ($a^* \sim 0.97$), perhaps indicating that even when allowing the height of the X-ray source to vary the data still want an evolution in the inner radius of the disk at some level. In both of these scenarios, we present the results for the high spin solution (which in the latter case gives a fit of $\chi^2/{\rm DoF} = 10678/10312$) because our subsequent modeling of the individual flares strongly suggests that the black hole in V404 Cyg is rapidly rotating (see Section 4.3). However, for completeness, we also present the parameter constraints for the lower-spin solutions in the Appendix; where the solutions are not the global best fit, errors are calculated as $\Delta\chi^2 = 2.71$ around the local χ^2 minimum. Separating out the solutions in this manner also allows the evolution required in $r_{\rm in}$ and h to be more clearly seen because both of these parameters are scaled by the spin in our model implementation. As expected, we see that either the inner radius of the accretion disk moves outward (Model 2), or the source height moves upward (Model 3), as the flux decreases. In Model 2, the inner disk radius evolves from the ISCO (assumed) out to $\sim 2.5\, r_{\rm ISCO}$, and in Model 3 the source height evolves from ~ 4 to $\sim 6\, r_{\rm H}$.

Finally, although the X-ray emission in the *NuSTAR* bandpass is clearly dominated by a hard, high-energy continuum and reprocessed emission, we also test for the presence of any thermal emission from an accretion disk. As the self-consistent evolutionary scenario that formally provides the best fit, we focus on the truncating disk scenario, and modify our model for the intrinsic emission from V404 Cyg to include a multi-color blackbody accretion disk (Model 4), using the DISKBB model (Mitsuda et al. 1984). In the XSPEC model outlined in Section 4.2.2, we thus update the source term

[15] Models that can also self-consistently compute $R_{\rm disk}$ for an X-ray source with a vertical outflow velocity are under development, but are not yet ready for publication, limiting our ability to test the third scenario of a variable source velocity.

Table 4
Results for the High-spin Solutions Obtained with the Lamp-post Reflection Models Constructed to Investigate Potential Geometric Evolution Scenarios As a Function of Flux (Models 2 and 3)

Model Component	Parameter		Global	Flux Level				
				F1	F2	F3	F4	F5
			Model 2: truncating disk, static corona					
RELXILLLP	Γ	...	...	$1.41^{+0.02}_{-0.03}$	$1.44^{+0.02}_{-0.03}$	1.40 ± 0.01	1.37 ± 0.02	1.37 ± 0.01
	$E_{\rm cut}$	(keV)	...	>540[a]	330 ± 60	190 ± 10	125^{+8}_{-6}	91^{+4}_{-3}
	a^*	...	>0.95	...	...	...	...	...
	i	(°)	36 ± 1	...	...	...	...	...
	h	($r_{\rm H}$)	$2.3^{+0.4}_{-0.1}$	...	...	...	...	...
	$A_{\rm Fe}$	(solar)	3.0 ± 0.1	...	...	...	...	...
	$r_{\rm in}$	($r_{\rm ISCO}$)	...	$2.5^{+0.4}_{-0.3}$	$2.3^{+0.1}_{-0.2}$	2.0 ± 0.1	$1.7^{+0.2}_{-0.1}$	1 (fixed)
	$R_{\rm disk}$[b]	...	...	1.3	1.5	1.7	1.9	3.0
	Norm	...	...	$0.61^{+0.11}_{-0.10}$	$0.80^{+0.18}_{-0.16}$	1.07 ± 0.15	$1.53^{+0.24}_{-0.31}$	$2.61^{+0.19}_{-0.51}$
χ^2/DoF			10656/10313					
			Model 3: stable disk, dynamic corona					
RELXILLLP	Γ	...	...	$1.36^{+0.03}_{-0.01}$	1.41 ± 0.01	$1.37^{+0.02}_{-0.01}$	1.36 ± 0.01	1.38 ± 0.01
	$E_{\rm cut}$	(keV)	...	540^{+80}_{-50}	280 ± 20	180 ± 10	123^{+5}_{-3}	94 ± 3
	a^*	...	>0.88	...	...	...	...	...
	i	(°)	28^{+1}_{-2}	...	...	...	...	...
	h	($r_{\rm H}$)	...	$5.2^{+1.5}_{-0.4}$	5.6 ± 0.3	$4.6^{+0.8}_{-0.2}$	$4.1^{+0.3}_{-0.2}$	4.4 ± 0.2
	$A_{\rm Fe}$	(solar)	3.03 ± 0.05	...	...	...	...	...
	$R_{\rm disk}$[b]	...	...	1.7	1.6	1.8	2.0	1.9
	Norm	...	...	0.18 ± 0.01	0.22 ± 0.01	$0.38^{+0.05}_{-0.01}$	$0.63^{+0.09}_{-0.04}$	$1.02^{+0.12}_{-0.07}$
χ^2/DoF			10678/10313					

Notes.
[a] $E_{\rm cut}$ is constrained to be $\leqslant$1000 keV following García et al. (2015).
[b] For these models, $R_{\rm disk}$ is calculated self-consistently in the lamp-post geometry from a^*, h, and $r_{\rm in}$. Because it is not a free parameter, errors are not estimated.

to be TBABS$_{\rm src}$ × (DISKBB + RELXILLLP). $R_{\rm disk}$ is still calculated self-consistently in the lamp-post geometry from a^*, h, and $r_{\rm in}$. During the fitting process for this model, we found that the DISKBB component only makes a significant contribution during the highest flux state (F5), and so fixed its normalization to zero for F1–4.

This model provides a good fit to the data, with $\chi^2/{\rm DoF} = 10581/10311$ (i.e., an improvement of $\Delta\chi^2 = 75$ for two additional free parameters over Model 2). We do not tabulate the parameter values because the vast majority have not varied significantly from the values presented for Model 2 in Table 4, but a few key parameters are worth highlighting individually. The best-fit disk temperature for the average flare spectrum is $0.41^{+0.10}_{-0.07}$ keV, such that this component only contributes close to the lower boundary of the *NuSTAR* bandpass. However, this temperature is similar to values reported from X-ray observatories with coverage extending to lower energies throughout this outburst (e.g., Radhika et al. 2016, Rahoui et al. 2017). The inclusion of this additional continuum component at the lower end of the *NuSTAR* bandpass allows the high energy power-law continuum to take on a harder photon index ($\Gamma = 1.32 \pm 0.01$), and subsequently a lower energy cutoff ($E_{\rm cut} = 75 \pm 4$ keV), such that this primary continuum emission exhibits stronger curvature in the *NuSTAR* band. In turn, this allows a slightly lower reflection fraction ($R_{\rm disk} = 2.5$), with the source height increasing slightly to $h = 2.5^{+0.5}_{-0.1}$ $r_{\rm H}$. The black hole spin remains high, with $a^* > 0.82$ (and noteably the χ^2 contour only displays a single solution; see Figure 9). The data/model ratios for the five flux states are shown in Figure 10 for this model, and the best-fit model along with the relative contributions of the various emission components are shown in Figure 11 for the highest flux state (F5).

It is worth noting that all of these flux-resolved models have returned inclinations for the inner disk of ~30°. This inclination would mark a large difference between the inclination of the inner disk and the orbital plane, which the latest optical studies during quiescence have estimated to be $i_{\rm orb} \sim 65°$ (Khargharia et al. 2010), with literature estimates covering a range from 50° to 75° (Shahbaz et al. 1994, 1996; Sanwal et al. 1996). While evidence of misalignment between the inner and outer regions of the disk has been seen in other sources, e.g., Cygnus X-1 (Tomsick et al. 2014; Walton et al. 2016), a difference this large would likely be unphysical (e.g., Fragos et al. 2010; Nealon et al. 2015). We will return to this issue in the following section.

4.3. Individual Flares

We also investigate a number of the individual flares, focusing on the six that reach or exceed ~10,000 ct s^{-1} (labeled in Figure 2). Following the reduction procedure used in Section 4.1, we extracted *NuSTAR* spectra for each of these six flares individually. These spectra are shown in Figure 12. While they are all reasonably similar, as suggested by their similar broadband hardness ratios (Figure 3), there are also obvious differences between them, so there is still some clear

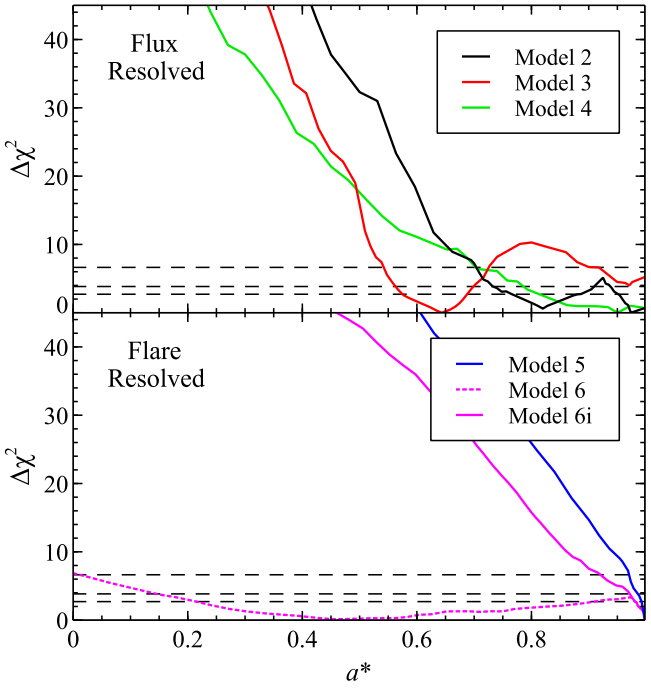

Figure 9. $\Delta\chi^2$ confidence contours for the black hole spin for our relativistic disk reflection models computed with a self-consistent lamp-post geometry. The top panel shows the models for our flux-resolved analysis (Models 2–4, see Section 4.2.3), while the bottom panel shows the models for our analysis of the strongest six flares individually (Models 5–6; see Section 4.3). For Model 6, we show both the contour calculated with no constraint on the inclination (dotted) and with the inclination constrained to $i \geqslant 50^\circ$ (solid; Model 6i) to match the estimates for the orbital plane of the binary system. The dashed horizontal lines indicate the 90%, 95%, and 99% confidence limits for one parameter of interest.

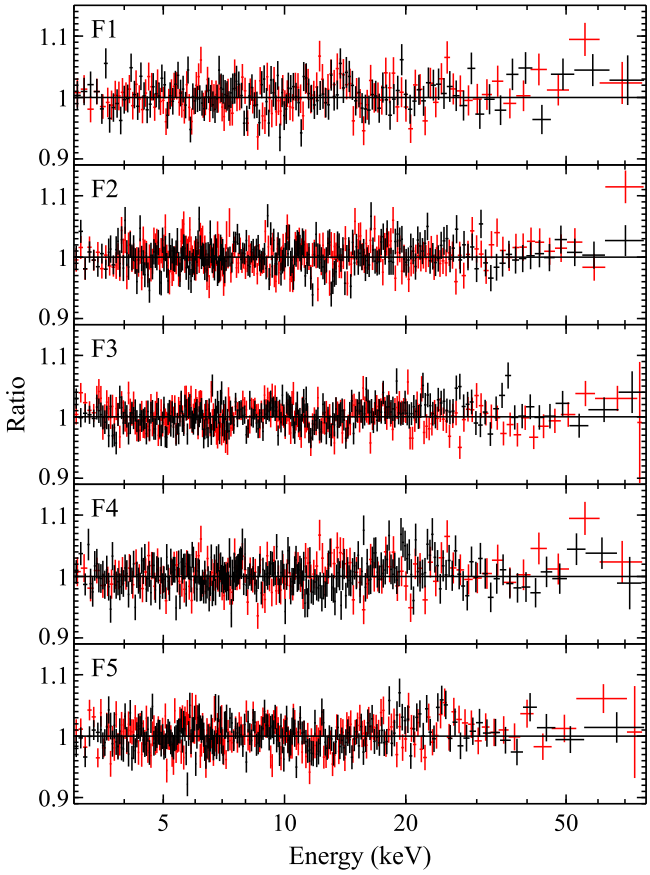

Figure 10. Data/model residuals for the truncating disk model with the thermal disk emission included from our flux-resolved analysis (Model 4; see Section 4.2.3). For each of the flux states, FPMA data are shown in black, and FPMB in red. As before, the data have been further rebinned for visual clarity.

averaging of different states in our flux-resolved analysis. For example, the first flare has a harder spectrum at lower energies than the subsequent flares, and the third flare has a softer spectrum than the rest over the *NuSTAR* bandpass.

We performed a joint fit of each of these flare spectra with the lamp-post model discussed in Sections 4.2.2 and 4.2.3 (excluding the photoionized emission component, which makes no contribution to the flux-resolved fits at high fluxes). As with our flux-resolved analysis, we link the black hole spin, iron abundance, accretion disk inclination, and ionization state of the photoionized absorption across all of the flares. Additionally, for the distant reprocessor, we fix the shape parameters (iron abundance, slab inclination) to the values found in the flux-resolved work. We also assume that the disk extends to the ISCO and again compute the reflection fraction self-consistently assuming a lamp-post geometry. Finally, given the results presented in Section 4.2.3, we fit the lamp-post model both with and without an accretion disk contribution, again using the DISKBB model. While fitting the model with the DISKBB component, we found the disk temperatures to be consistent among all of the flares, and so linked this parameter across the data sets for simplicity. The results obtained with both these models (Models 5 and 6, respectively) are presented in Table 5.

The pure lamp-post model (Model 5) fits the data well, with $\chi^2/\mathrm{DoF} = 6039/5859$. The spin is constrained to be very high, $a^* > 0.99$ (see Figure 9), and there is a slight increase in the

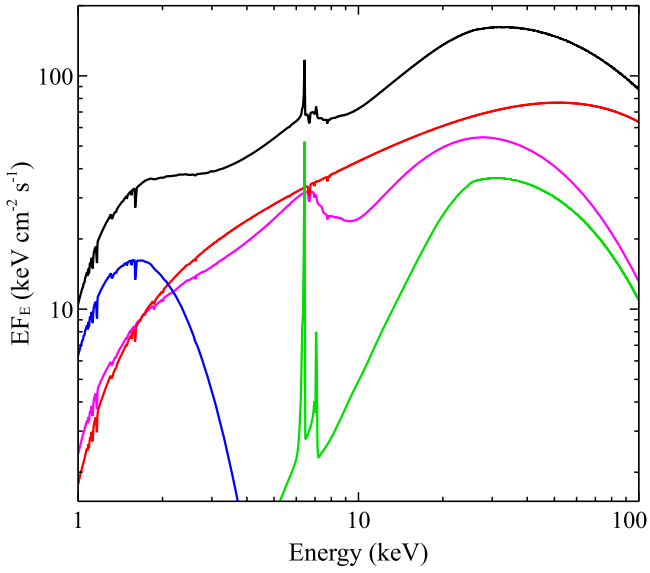

Figure 11. Best-fit disk reflection model obtained for the flare spectrum (F5) from Model 4 in our flux-resolved analysis (the truncating disk model with the thermal disk emission included). The total model is shown in black, and the relative contributions from the accretion disk (blue), the high-energy power-law tail (red), the disk reflection (magenta) and the distant reflection (green) are also shown.

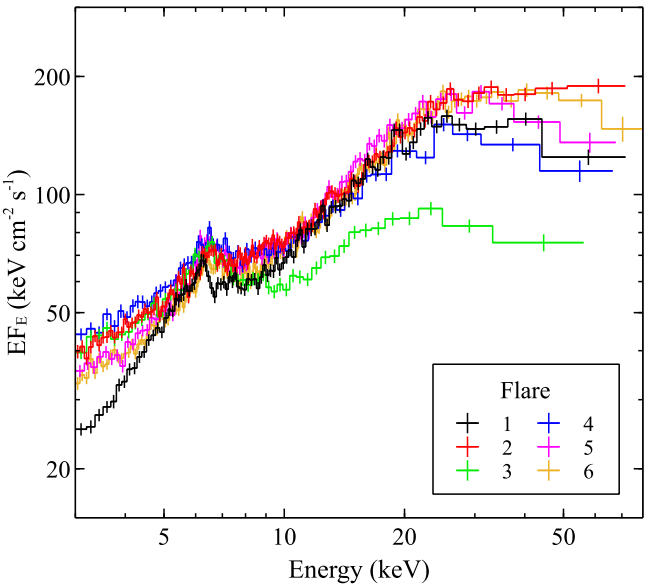

Figure 12. X-ray spectra extracted from the six major flares highlighted in Figure 2 (Flares 1–6 shown in black, red, green, blue, magenta, and orange, respectively). Same as in Figure 7, only the FPMA data are shown for clarity, and the data have been unfolded through a constant and rebinned for visual purposes. While the flares all show similar broadband hardness ratios (Figure 3), there are clear differences between them. For example, Flare 1 (black) shows a harder spectrum at lower energies, and Flare 3 (green) shows a softer spectrum than the rest.

inclination inferred for the inner disk; while the flux-resolved analysis typically found $i \sim 30°$, here we find $i \sim 40°$. We find that the first flare shows stronger absorption than the subsequent flares, both in terms of the neutral and the ionized absorption components. The former results in the harder spectrum seen from this flare at lower energies, and there is a clear absorption line from ionized iron at ∼6.7 keV produced by the latter, similar to that reported by King et al. (2015), which is not seen in any of the subsequent flares. As with the flux-resolved analysis, we find that during the flares the height inferred for the X-ray source is very close to the black hole, always within $\sim 10\, r_G$.

The model including the disk emission (Model 6) again provides a substantial improvement over the basic lamp-post model, resulting in an outstanding fit to the data ($\chi^2/\mathrm{DoF} = 5906/5852$, i.e., an improvement of $\Delta\chi^2 = 133$ for seven additional free parameters). We show the data/model ratios for the individual flares with this model in Figure 13. The disk temperature is again similar to that reported by lower energy missions, $T_{\rm in} \sim 0.5$ keV, and as before we see that the inclusion of this emission allows the high-energy continuum to take on a harder form, subsequently resulting in lower-energy cutoffs. The neutral absorption inferred also increases to compensate for this additional low-energy continuum emission.

With regards to the black hole spin, we again find a situation in which two solutions exist that provide statistically equivalent fits (separated by $\Delta\chi^2 < 1$; see Figure 9): one at high spin ($a^* > 0.98$), which is marginally preferred, and another broad, local minimum at a more moderate spin ($a^* \sim 0.5$). In this case, the dual solutions are related to a significant degeneracy between the spin and the disk inclination, resulting from the combination of the additional continuum component, and the lower total S/N utilized in these fits (these data represent ∼80% of the exposure from which the F5 spectrum considered in the previous section is extracted).

For the best-fit, high spin solution we find that the inclination has further increased to $i \sim 52°$, which is similar to the estimates for the orbital inclination of the system ($i_{\rm orb} \sim 50°$–$75°$; e.g., Shahbaz et al. 1994; Khargharia et al. 2010). In contrast, for the more moderate-spin solution, we find that the associated inclination is $<20°$. This would imply an even more extreme disk warp than the flux-resolved analysis, which we deem unphysical. This degeneracy between the spin and the inclination is distinct from the traditional sense of a parameter degeneracy, in which two parameters are correlated such that any value of one can be made acceptable by adjusting the other; rather, there are two solutions that are acceptable in distinct areas of parameter space. We therefore present the results from the high-spin solution in Table 5, though again the parameter constraints for the lower-spin solution are presented in the Appendix, and recalculate the confidence contour for the black hole spin with the inclination constrained to be $i \geqslant 45°$ for this model (which we refer to as Model 6i; see Figure 9) in order to ensure a reasonable agreement between the inner and outer disk. This constraint strongly requires a rapidly rotating black hole. We also assess the degree to which the assumed geometry is driving the spin constraint in this scenario by relaxing the requirement that $R_{\rm disk}$ is set self-consistently and allowing this to vary as a free parameter for each of the six flares (but keeping the $i \geqslant 45°$ constraint). Although the constraint on the spin is naturally looser, we still find that $a^* > 0.7$ and the constraints on $R_{\rm disk}$ are all consistent with the values presented in Table 5. If we exclude unphysically large disk warps, a rapidly rotating black hole is still required regardless of any additional geometric constraints.

The range of heights inferred for the X-ray source remains similar to the pure lamp-post case. However, one issue of note with this model is that the iron abundance has increased to $A_{\rm Fe}/\mathrm{solar} \sim 5$ (for both solutions), in order to compensate for the harder irradiating continuum and reproduce the observed line flux. All our previous models had typically found $A_{\rm Fe}/\mathrm{solar} \sim 2$–3, which is similar to the iron abundance of $A_{\rm Fe}/\mathrm{solar} \sim 2$ found for the companion star by González-Hernández et al. (2011). While this is certainly not always the case (e.g., El-Batal et al. 2016), similarly high iron abundances have also been reported for a few other Galactic BHBs observed by *NuSTAR* when using the XILLVER based family of reflection models (e.g., Fuerst et al. 2016; Parker et al. 2016; Walton et al. 2016). The abundance inferred may be dependent on the reflection code utilized; Walton et al. (2016) note that for the Galactic binary Cygnus X-1, the iron abundances obtained with the XILLVER family of reflection models are generally a factor of ∼2 larger than those obtained with the REFLIONX (Ross & Fabian 2005) family of models (see also Miller et al. 2015). Should the iron abundance here be systematically overpredicted by a similar factor, this would bring the abundance derived back down to $A_{\rm Fe}/\mathrm{solar} \sim 2.5$, which would again be similar to that reported by González-Hernández et al. (2011). However, we stress that the key results obtained here do not strongly depend on this issue. If we fix the iron abundance to $A_{\rm Fe}/\mathrm{solar} = 2$ in Model 6, the fit worsens slightly (but is still excellent, $\chi^2/\mathrm{DoF} = 5933/5853$). The spin is strongly constrained to be very high ($a^* > 0.997$), and the requirement for small

Table 5
Results Obtained for the Free Parameters in the Lamp-post Reflection Models Constructed for the Joint Fits to the Individual Flare Spectra (Models 5 and 6)

Model Component	Parameter		Global	Flare					
				1	2	3	4	5	6
Model 5: lamp-post only									
TBABS$_{src}$	N_H	(10^{22} cm^{-2})	...	$3.3^{+0.6}_{-0.8}$	<0.2	<0.3	<0.2	<0.1	<0.1
RELXILLLP	Γ	...	...	$1.22^{+0.06}_{-0.12}$	$1.44^{+0.01}_{-0.03}$	$1.63^{+0.08}_{-0.12}$	$1.52^{+0.03}_{-0.04}$	$1.28^{+0.02}_{-0.03}$	$1.58^{+0.01}_{-0.03}$
	E_{cut}	(keV)	...	50^{+6}_{-10}	210 ± 30	47 ± 4	94^{+12}_{-15}	60^{+4}_{-6}	140^{+20}_{-10}
	a^*	...	>0.99	...	...	...	...	...	...
	i	(°)	42 ± 2	...	...	...	...	...	...
	h	(r_H)	...	<2.2	<2.4	$4.0^{+3.5}_{-1.0}$	$2.7^{+1.6}_{-0.3}$	<2.1	$8.0^{+3.3}_{-0.9}$
	A_{Fe}	(solar)	$2.9^{+0.3}_{-0.6}$	...	...	...	...	...	...
	$\log \xi$	log (erg cm s^{-1})	...	3.2 ± 0.1	$3.5^{+0.2}_{-0.1}$	$3.1^{+0.2}_{-0.1}$	$3.4^{+0.2}_{-0.1}$	$3.36^{+0.07}_{-0.05}$	2.2 ± 0.1
	R_{disk}[a]	...	...	5.3	4.4	2.3	3.4	5.3	1.5
	Norm	...	...	$4.2^{+0.3}_{-0.5}$	$4.4^{+0.9}_{-0.7}$	$1.1^{+0.3}_{-0.4}$	$2.1^{+0.5}_{-1.1}$	$3.9^{+0.3}_{-1.2}$	1.3 ± 0.2
XSTAR$_{abs}$	$\log \xi$	log (erg cm s^{-1})	$5.3^{+0.4}_{-0.3}$	...	...	...	...	...	...
	N_H	(10^{21} cm^{-2})	...	43^{+12}_{-10}	<1	<3	<7	<3	<12
XILLVER	Norm	...	...	0.22 ± 0.04	$0.42^{+0.09}_{-0.08}$	0.25 ± 0.06	$0.34^{+0.04}_{-0.07}$	0.45 ± 0.05	0.40 ± 0.04
χ^2/DoF			6039/5859						
Model 6: lamp-post with disk emission									
TBABS$_{src}$	N_H	(10^{22} cm^{-2})	...	$5.1^{+1.0}_{-1.1}$	$2.3^{+0.9}_{-0.6}$	$3.6^{+1.4}_{-1.3}$	$2.2^{+1.5}_{-1.3}$	$3.3^{+1.1}_{-1.0}$	$3.8^{+0.8}_{-0.9}$
DISKBB	T_{in}	(keV)	0.49 ± 0.04	...	...	...	...	...	...
	Norm	(10^5)	...	$1.5^{+1.3}_{-0.7}$	$1.9^{+1.5}_{-1.1}$	$3.4^{+2.9}_{-1.5}$	$2.2^{+1.4}_{-1.1}$	$2.7^{+2.2}_{-1.2}$	$2.8^{+1.9}_{-1.2}$
RELXILLLP	Γ	...	...	<1.04[b]	$1.27^{+0.04}_{-0.03}$	$1.29^{+0.12}_{-0.08}$	$1.33^{+0.07}_{-0.06}$	<1.12[b]	$1.22^{+0.06}_{-0.04}$
	E_{cut}	(keV)	...	40^{+3}_{-2}	113^{+16}_{-28}	32^{+5}_{-4}	60^{+12}_{-9}	42^{+5}_{-3}	68^{+8}_{-6}
	a^*	...	>0.98	...	...	...	...	...	...
	i	(°)	52^{+2}_{-3}	...	...	...	...	...	...
	h	(r_H)	...	<2.3	<3.8	<3.6	<3.5	<2.4	$7.5^{+8.7}_{-1.9}$
	$\log \xi_{disk}$	log (erg cm s^{-1})	...	3.5 ± 0.1	3.8 ± 0.1	3.4 ± 0.1	3.6 ± 0.1	3.6 ± 0.1	3.5 ± 0.1
	A_{Fe}	(solar)	$5.0^{+0.7}_{-0.4}$	...	...	...	...	...	...
	R_{disk}[a]	...	...	5.3	3.9	4.1	4.1	5.3	1.6
	Norm	...	...	$3.5^{+0.2}_{-0.8}$	$3.1^{+2.0}_{-1.7}$	$1.9^{+1.0}_{-0.9}$	$2.7^{+1.4}_{-1.3}$	$3.5^{+0.2}_{-1.2}$	$1.0^{+0.4}_{-0.2}$
XSTAR$_{abs}$	$\log \xi$	log (erg cm s^{-1})	5.7 ± 0.2	...	...	...	...	...	...
	N_H	(10^{21} cm^{-2})	...	88^{+4}_{-3}	<6	<16	<30	<23	19^{+17}_{-11}
XILLVER	Norm	...	...	0.13 ± 0.05	$0.22^{+0.09}_{-0.08}$	0.13 ± 0.07	0.19 ± 0.09	0.29 ± 0.06	$0.26^{+0.06}_{-0.03}$
χ^2/DoF			5906/5852						
F_{3-79}[c]	(10^{-8} erg cm^{-2} s^{-1})		...	50.7 ± 0.6	62.4 ± 0.6	34.4 ± 0.5	50.6 ± 0.6	57.0 ± 0.6	60.0 ± 0.4

Notes. For model 6, the high-spin solution is given.
[a] For these models, R_{disk} is calculated self-consistently in the lamp-post geometry from a^* and h. Because it is not a free parameter, errors are not estimated.
[b] The RELXILLLP model is only calculated for $\Gamma \geqslant 1$.
[c] Average flux in the 3–79 keV bandpass.

source heights further tightens. The most noteable change is that the best-fit inclination further increases to $i \sim 60°$, which is still in good agreement with the range estimated for the orbital plane.

The 3–79 keV fluxes observed from these spectra are also given in Table 5. However, the average count rates during the periods from which these spectra are extracted are obviously significantly lower than the peaks of the flares. Assuming a similar spectral form, scaling these fluxes up to the peak incident count rates observed during these flares—as determined from light curves with 1s time bins—corresponds to peak 3–79 keV fluxes ranging from $0.8–2.0 \times 10^{-6}$ erg cm^{-2} s^{-1}. For a $10\,M_\odot$ black hole at a distance of 2.4 kpc, these fluxes equate to 3–79 keV luminosities of $\sim$0.4–1.0 L_E (where $L_E = 1.4 \times 10^{39}$ erg s^{-1} is the Eddington luminosity). The bolometric fluxes observed from the DISKBB component in these spectra, which assumes a thin disk as described by Shakura & Sunyaev (1973), equate to disk luminosities of $\sim$0.1 L_E (assuming the disk is viewed close to $i \sim 60°$). Temperatures of $T_{in} \sim 0.5$ keV are not unreasonable for such luminosities (e.g., Gierliński & Done 2004; Reynolds & Miller 2013). Assuming these fluxes also scale up during the peaks of the flares, the peak disk fluxes would equate to luminosities of $\sim$0.3–0.5 L_E.

4.4. Evolution across Flare 4

As the final component of our analysis in this work, we track the evolution of the spectrum across one of the major flares considered in Section 4.3. We focus on Flare 4 (see Figure 2)

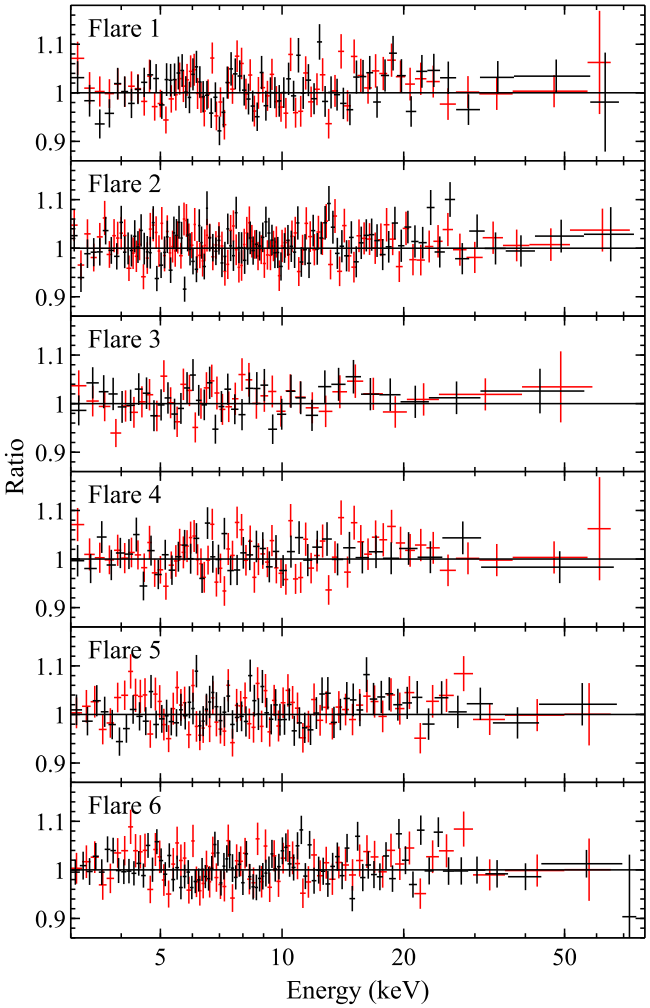

Figure 13. Data/model residuals for the lamp-post reflection model with the thermal disk emission included from our flare-resolved analysis (Model 6; see Section 4.3). Again, for each of the flares, the FPMA data are shown in black and the FPMB data in red, and the data have been further rebinned for visual clarity.

because it is followed by a relatively long, uninterrupted period of low absorption (as determined by our analysis in Section 4.2.1). As such, we should have a relatively clean view of the flare and its subsequent decline. In order to track the evolution of the spectrum, we split the data into bins with 40 s durations, and extracted spectra from each, again following the method outlined in Section 2. While significant variability obviously occurs on shorter timescales (e.g., P. Gandhi et al. 2017, in preparation), a 40 s duration was found to offer a good balance between retaining good time resolution and the need for reasonable S/N in the individual spectra. We start immediately prior to the flare, and continue until the point that the observed count rate (as averaged over 40 s) starts to rise again after the decline of the flare, resulting in 14 time-resolved spectra (per FPM) in total (hereafter T1–14). These spectra are shown in Figure 14.

There are too many data sets to undertake a joint analysis of all the data, so we fit the data from each of the time bins individually, using the same lamp-post-based model utilized in our joint analysis of the major flares observed (Section 4.3). Specifically, we use the model that includes the thermal disk emission (Model 6). However, the average good exposure time per FPM is only ∼11 s per bin (being higher for lower flux bins and vice versa, owing to the instrumental deadtime; Harrison et al. 2013), so the S/N per time bin is relatively low. We therefore limit ourselves to considering only a few key free parameters when fitting each of these data sets. Because there is no evidence for ionized iron absorption during this flare (only an upper limit is obtained on the column for this component during flare 4, see Table 5), we exclude the XSTAR absorption component from our analysis in this section. Furthermore, we fix all of the remaining global parameters (black hole spin, disk inclination, iron abundance, and disk temperature) to the best-fit values presented for Model 6 in Table 5. We also fix the ionization parameter to the value obtained in our flux-resolved analysis (see Table 3), based on the average count rate in that time bin, thus ensuring that the ionization increases as the flux increases. Finally, we are not able to simultaneously constrain both the inner radius of the disk and the height of the X-ray source, so we initially fix the latter at the best fit obtained for this flare in our flare-resolved analysis ($h = 2.5\ r_{\rm H}$). The free parameters allowed to vary for each of the time-resolved data sets are therefore the (source intrinsic) neutral absorption column, the photon index and high-energy cutoff of the power-law continuum, the inner radius of the disk, and the normalizations of the various emission components. As before, the reflection fraction $R_{\rm disk}$ is calculated self-consistently from the spin, source height, and inner radius of the disk in the lamp-post geometry, which helps us to constrain $r_{\rm in}$ in these fits.

The results for a number of the key parameters, as well as a zoom-in on the light curve of this flare, are shown in Figure 15, which shows a characteristic fast rise, exponential decay profile. Aside from the first time bin, the absorption stays relatively low and stable throughout, as expected. Prior to the flare, the observed spectrum is relatively soft (in comparison to the spectra shown in Figures 7 and 12). Then, as the source flares, the spectrum hardens significantly (reaching $\Gamma = 1.14^{+0.04}_{-0.08}$), and during the decline it softens again before gradually becoming harder as the source fades. We see a significant difference in the average cutoff energy before and after the flare. Finally, we also see a significant difference in the inner radius of the disk, the key geometry parameter in this analysis, across the evolution of the flare, being close to the ISCO prior to and during the rise of the flare, before moving out to $\sim 10\, r_{\rm ISCO}$ during the subsequent decline. The data are well modeled, with an average χ^2/DoF of 1.02 (for an average of 302 DoF). As a sanity check, assuming a disk structure of $h_{\rm D}/r_{\rm D} \sim 0.2$ (where $h_{\rm D}$ is the scale height of the disk at a given radius $r_{\rm D}$; see Section 5.2), a standard viscosity parameter of $\alpha \sim 0.1$, and that the dynamical timescale is set by the Keplerian orbital timescale, we estimate that the viscous timescale for the disk should be ∼0.01 s at a radius of $10\, r_{\rm G}$ (for our best-fit spin, $r_{\rm ISCO} \sim r_{\rm G}$) for V404 Cyg. Significant evolution of the inner disk is therefore certainly possible over the timescales probed here.

We also consider two additional iterations of this analysis. First, as with our flux-resolved analysis, we also consider the case in which h varies and $r_{\rm in}$ stays constant, fixing the latter to the ISCO throughout. Equivalent results are obtained, with the only difference being that h increases as the flare evolves instead of $r_{\rm in}$, starting at $\sim 2\, r_{\rm H}$ before jumping to $\sim 20\, r_{\rm H}$ in the decline of the flare. The fit statistics are very similar to the

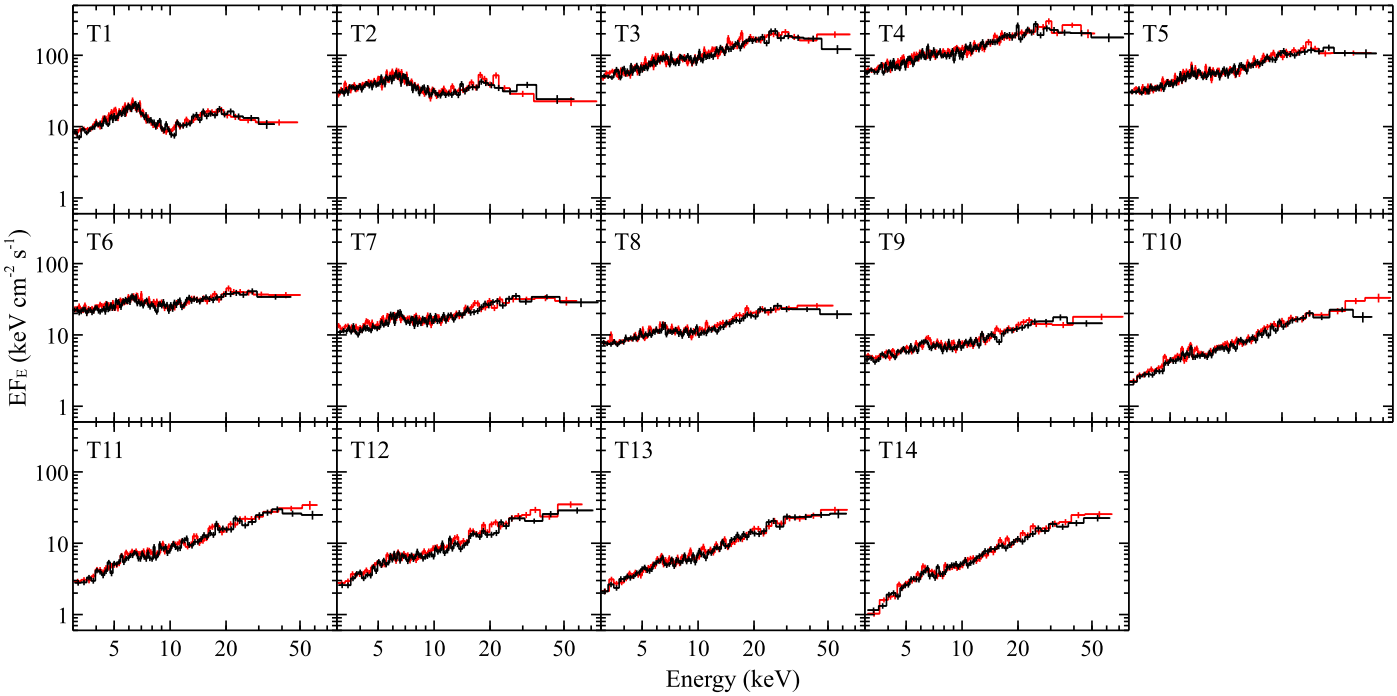

Figure 14. Fourteen time-resolved X-ray spectra extracted across the evolution of flare 4 (labeled T1–14). As before, the data have been unfolded through a constant and rebinned for visual purposes, and the FPMA and FPMB data are shown in black and red, respectively. Significant spectral changes are seen as the source flares and then decays.

scenario in which $r_{\rm in}$ varies and h is constant. At least one of h or $r_{\rm in}$ must therefore increase across the flare; in reality, the two may evolve together. Second, we relax our assumption with regards to the ionization of the disk. While this would be expected to increase with increasing luminosity for a constant density, with the inner regions of the disk evolving its density may also vary. We therefore re-fit the data with the ionization as a further free parameter. While this increases the uncertainties on the other parameters, the same qualitative evolution is still seen, with the main difference being that the point at which $r_{\rm in}$ moves outward occurs later in time. Broadly speaking, the ionization of the disk does still appear to increase with increasing flux.

Finally, we note that V404 Cyg is known to exhibit a strong dust halo, which can produce emission that can potentially mimic an accretion disk component, particularly when the source is faint (Beardmore et al. 2016; Heinz et al. 2016; Motta et al. 2016; Vasilopoulos & Petropoulou 2016). However, during this work, we are largely focusing on periods when the source was very bright. Furthermore, in the analysis presented here, we find that the normalization of the DISKBB component included in the model varies across Flare 4 along with the overall flux. This is too fast for the response from dusty interstellar clouds, and so we cannot be mistaking a dust contribution for the accretion disk in this work.

5. Discussion

We have undertaken an analysis of the first of a series of *NuSTAR* observations of V404 Cyg taken across its recent outburst in summer 2015. This observation was taken during the period of extreme activity from the source (see Figure 1). Extreme flux and spectral variability is present throughout (see Figure 2), driven in part by strong and variable line-of-sight absorption, similar to that seen in the last major outburst from this source in 1989 (e.g., Zycki et al. 1999a). We also see a period of intense flaring, similar to that reported by other high-energy observatories (e.g., King et al. 2015; Natalucci et al. 2015; Rodriguez et al. 2015; Roques et al. 2015; Jenke et al. 2016), with the source reaching observed fluxes that correspond to its Eddington luminosity in the 3–79 keV band in the most extreme cases covered by *NuSTAR*. Given the strength of these flares, the ability of *NuSTAR* to cleanly observe extreme count rates free of instrumental effects such as pile-up, owing to its triggered read-out (Harrison et al. 2013), has been critical to this work.

Our analysis focuses primarily on this flaring period. While the line-of-sight absorption is often strong during this observation, as indicated by the strong edge seen at $\sim$7 keV in the average spectrum from the entire observation (see Figure 4), the average spectrum extracted from the highest fluxes (the flare peaks) seen during this period shows comparatively little absorption, with no strong edge seen, and thus offers us a relatively clean view of the intrinsic spectrum from V404 Cyg. These data show clear evidence of relativistic reflection from an accretion disk (Figure 5), as well as reprocessing from more distant material (see also King et al. 2015; Motta et al. 2016). We undertake a series of detailed analyses in order to determine the relative contributions of these components, and probe the geometry of the inner accretion flow during these flares.

First, we use these flares as a template to identify further periods of low absorption throughout the rest of the *NuSTAR* observation, and undertake a flux-resolved analysis of these data (Section 4.2), averaging them into five flux bins and fitting these simultaneously with the latest self-consistent disk reflection model, assuming a lamp-post geometry

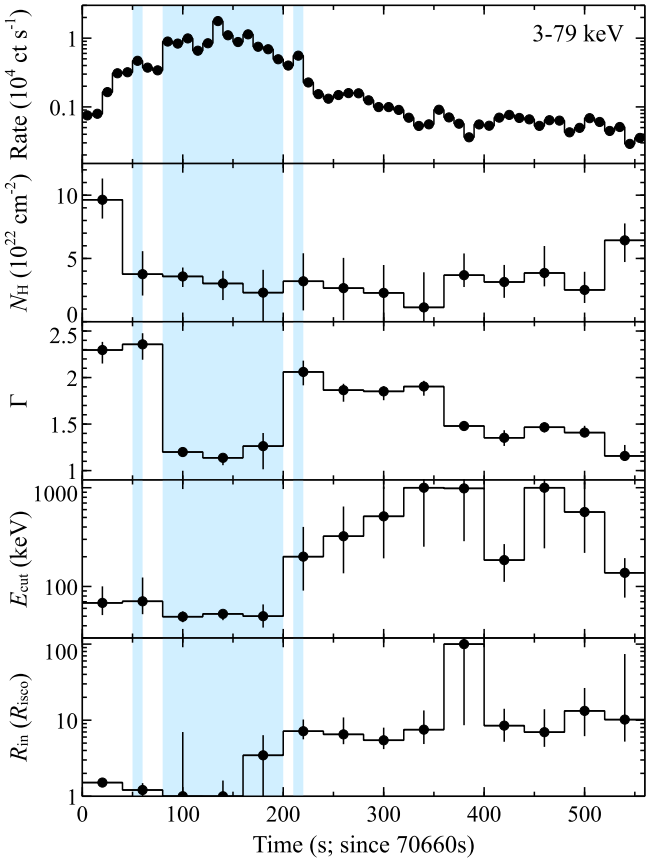

Figure 15. Results for the key lamp-post model parameters obtained with our time-resolved spectral analysis of Flare 4, in this case, allowing the inner radius of the disk to vary while holding the height of the X-ray source constant (see the text). The top panel shows the light curve around flare 4 (10 s bins), while the lower panels show the evolution of the intrinsic neutral absorption column, the photon index and high-energy cutoff of the power-law continuum, and the inner disk radius, respectively (each 40 s bins). The high-energy continuum hardens significantly during the peak of the flare. In addition, both the high-energy cutoff and the inner radius of the disk are significantly larger after the peak of the flare than before. The shaded regions indicate periods when the count rate exceeds 4000 ct s^{-1}, which contribute to the Flare 4 spectrum shown in Figure 12.

(RELXILLLP; García et al. 2014). The relative contribution of the disk reflection decreases with decreasing flux. The evolution of the strength of the disk reflection implies that, on average, the solid angle subtended by the disk, as seen by the illuminating X-ray source, decreases with decreasing flux. In turn, this requires an evolution in the geometry of the innermost accretion flow. To minimize parameter degeneracies, we tested two limiting scenarios based on an idealized lamp-post approximation for the accretion geometry, first in which the changing solid angle is explained with a truncating disk and a static illuminating source, and second with a stable disk and a changing source height (resulting in a varying degree of gravitational light bending). The latter scenario could potentially represent either a physical motion or a vertical expansion of the X-ray source. We note, however, that it is possible (if not likely, as discussed below) that both the inner radius of the disk and the height of the X-ray source could be varying simultaneously. Both of the scenarios considered suggest that during the peaks of the flares, the average position of the X-ray source is close to the black hole ($h \lesssim 5\ r_G$). In addition to the high-energy power-law continuum and the reprocessed emission components that dominate the majority of the *NuSTAR* band, we also find evidence for a weak contribution from thermal emission from the disk in the highest flux bin, seen at the lowest energies probed (see Figure 11). The lower flux data do not show any evidence for such emission in the *NuSTAR* band.

Second, we undertake a joint analysis of the spectra extracted from the peaks of the six strongest flares observed (highlighted in Figure 1; Section 4.3). We again fit the data with our lamp-post disk reflection model in order to build on our previous analysis and probe the geometry during these flares individually. While these flares all have broadly similar spectra, there are also differences between them (Figure 12), so it is important to assess what effect the averaging of different spectra inherent to our flux-resolved analysis might have on the results obtained. Our analysis of these data with our lamp-post disk reflection model finds further support for the contribution of thermal disk emission at the highest fluxes, and also confirms that the X-ray source is indeed close to the black hole (within $\sim 10\, r_G$) during these flares.

With the strong gravitational light bending associated with this regime resulting in an increased fraction of the emitted flux being lost over the black hole horizon and/or bent onto the accretion disk, the intrinsic power emitted during these flares would be even larger than simply inferred from the observed fluxes. For the high spin solutions, the work of Dauser et al. (2014) suggests that only ∼20% of the intrinsically emitted flux should be lost over the event horizon, so the reflection fraction—defined here to be the ratio of the fluxes seen by the disk and by the observer—provides a reasonably good scaling factor between the observed and intrinsic fluxes. At the flare peaks, we would therefore infer the hard X-ray continuum to be intrinsically ∼4 times brighter (on average) than observed based on our flare-resolved analysis. However, we stress that this correction is geometry dependent, and even within the assumed geometry depends strongly on the source height; increasing h within the formal statistical uncertainties quoted in Table 5 can reduce this factor quite substantially (by up to ∼40%).

Finally, we undertake a time-resolved analysis of the evolution across one of these major flares, focusing on flare 4 (Section 4.4). Spectra are extracted every 40 s, and fit individually with our lamp-post disk reflection model. Owing to the short exposures, the S/N in each spectrum is relatively poor. We therefore again focus on the limiting scenarios in which the inner radius of the disk varies while the height of the X-ray source remains constant, and vice versa (though we again stress that this is for pragmatic reasons regarding parameter degeneracies, and that both quantities may in reality vary together, as discussed below). In both cases, we find clear differences before and after the peak of the flare, so at least one of these quantities must evolve across the flare; either the disk truncates, or the height of the source increases (Figure 15). During the peak of the flare, the primary continuum is extremely hard ($\Gamma \sim 1.1$), and we also see a clear evolution in the high-energy cutoff, which is significantly higher after the peak of the flare than it was before.

5.1. Jet Activity

We suggest that the strong flares observed by *NuSTAR* mark transient jet ejection events, with the jet becoming the source of the X-rays illuminating the disk (hence our use of the lamp-post

geometry throughout our reflection modeling). There are a variety of lines of evidence from the X-ray band alone that support this claim. In other accreting black holes, strong X-ray flares are known to be associated with such events. The BHB XTE J1550-564 is particularly notable in this respect. During its 1998 outburst, an approximately Eddington level flare was observed by *RXTE*, which triggered the onset of super-luminal radio ejecta, and some time later ejecta were resolved from the central point source by *Chandra* (Corbel et al. 2002; Kaaret et al. 2003; Tomsick et al. 2003; Steiner & McClintock 2012). Such behavior has also been seen from the BHB H 1743−322 (Corbel et al. 2005; McClintock et al. 2009; Steiner et al. 2012), and the X-ray flux seems to be elevated in the hours prior to many of the radio ejections from the BHB GRS 1915+105 (e.g., Punsly & Rodriguez 2013; Punsly et al. 2016). In addition, some X-ray flares in active galaxies also appear to be associated with jet ejection events (e.g., the recent flares observed from Mrk 335 and M81; Wilkins et al. 2015; King et al. 2016). The fact that the intrinsic spectrum observed immediately prior to flare 4 in our time-resolved analysis is inferred to be quite soft ($\Gamma \sim 2.3$) is of potential importance here, because this is very similar to the "steep power-law state" identified by Remillard & McClintock (2006 also referred to as the "Very High State" in other works). For most LMXBs in outburst, transient jets are launched as they flare up to approximately Eddington during the transition from the hard state to the soft state, which occurs via the steep power-law state (e.g., Corbel et al. 2004; Fender et al. 2004; Steiner et al. 2011; Narayan & McClintock 2012).

In addition to this broader precedent, the nature of the X-ray spectrum observed during these flares also supports a jet scenario. Even after accounting for the reprocessed emission, the primary X-ray continuum is found to be extremely hard, despite the high flux; on average, we see $\Gamma \sim 1.4$, and from our time-resolved analysis of flare 4, we see that the continuum even reaches $\Gamma \sim 1.1$. This is not the spectrum that would be expected from an accretion flow radiating at approximately Eddington, which should be dominated by emission from a multi-color blackbody accretion disk, modified slightly by the effects of photon advection (e.g., Middleton et al. 2012, 2013; Straub et al. 2013). In addition, spectra this hard (particularly in the $\Gamma \sim 1.1$ case) are difficult to produce via Compton scattering of thermal disk photons in a standard accretion disk corona. Strong illumination of the corona by the disk should cool the electrons and produce a softer spectrum. The hard X-ray source would therefore be required to be extremely photon starved (e.g., Fabian et al. 1988; Haardt & Maraschi 1993), in which case only a very small fraction of the disk emission would be scattered into the hard X-ray continuum, or some other process must serve to counteract the cooling of the electrons.

This may point to a magnetic origin for the flares, which would also support a transient jet scenario (e.g., Dexter et al. 2014). Furthermore, if we assume that immediately prior to this flare the high-energy continuum is produced by thermal Comptonization, following a similar calculation to Merloni & Fabian (2001) and taking h to be representative of the size-scale of the corona, we find that there is not enough thermal energy stored in the corona to power the flare by many orders of magnitude, which would also support a magnetic origin. While the spectrum during the peak is also likely too hard for direct synchrotron emission from a jet, which would be expected to give $\Gamma \sim 1.7$ in the X-ray band, but synchrotron-self-Compton emission (e.g., Markoff et al. 2005) may be able to produce a high-energy continuum this hard.

The increase of roughly an order of magnitude in $E_{\rm cut}$ observed across flare 4, from ∼50 to ∼500 keV, would also appear to indicate that significant energy is being injected into the X-ray emitting electron population during this event, because $E_{\rm cut}$ is a proxy for the electron temperature $T_{\rm e}$. *INTEGRAL* may have seen a similar evolution in the cutoff across one of the bright flares observed during its coverage of this outburst (Natalucci et al. 2015). If the height of the source does increase across this flare, the change in gravitational redshift experienced by the primary emission could contribute at least in part to the difference seen in $E_{\rm cut}$, since this correction is not yet incorporated into the RELXILLLP model (Niedźwiecki et al. 2016). However, in the most extreme scenario, where $r_{\rm in}$ remains constant while h varies (evolving from ∼2 to ∼20 $r_{\rm G}$), the movement of the source height should only result in a factor of ∼2 change in the observed cutoff energy (assuming no intrinsic variation). This is clearly insufficient to explain the difference observed, and so we conclude that the intrinsic cutoff energy does indeed increase across the flare.

Assuming the power-law emission is produced by Compton scattering at least during the times both prior to and after the main flare, this implies either an increase in the characteristic electron temperature if the particle distribution remains thermal, or perhaps a transition to a more power-law-like (non-thermal) distribution that extends up to significantly higher energies. With the spectral coverage of *NuSTAR* stopping at 79 keV, it can be difficult to distinguish between these two scenarios for sufficiently high electron temperatures in the thermal case, because the high-energy cutoff is shifted out of the *NuSTAR* bandpass, resulting in the observation of a power-law spectrum with little or no curvature. In turn, this results in a run-away effect in terms of the measured $E_{\rm cut}$, owing to the fact that the cutoff power-law model is constantly curving at all energies, while a thermal Comptonization continuum is more power-law-like until it rolls over with a sharper cutoff (see the discussion in Fürst et al. 2016), potentially explaining the fact that $E_{\rm cut}$ is often consistent with the maximum value currently permitted by the RELXILL models after the flare. Nevertheless, the evolution in $E_{\rm cut}$ observed here provides a good match to the jet model described in Markoff et al. (2005), in which electrons are accelerated into a power-law distribution within a region of ∼10–100 $r_{\rm G}$ above the jet's point of origin. Should the particle distribution instead be thermal both before and after the peak of the flare, assuming that the size of the corona increases across the flare (i.e., it expands as either $r_{\rm in}$ or h increase), then the evolution would be similar to that expected for a corona being kept close to its catastrophic pair production limit (see Fabian et al. 2015, and references therein).

Finally, the geometric results from our reflection modeling are also likely consistent with a jet scenario. We see evidence for either the disk truncating or the height of the X-ray source increasing, both on average as the source flux decreases, and also across one of the major flares individually. Although we cannot constrain the evolution of the inner disk radius and the source height simultaneously, as variations in the two produce similar results for the observed reflection spectrum (e.g., Fabian et al. 2014, hence our treatment of these two

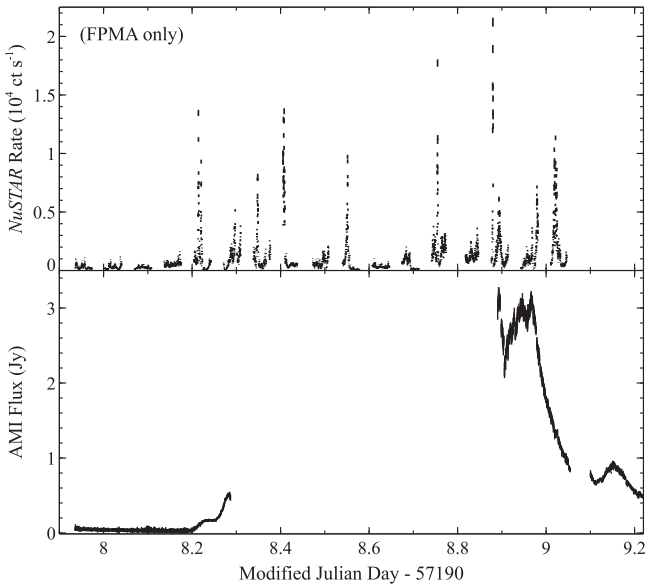

Figure 16. Comparison of the *NuSTAR* light curve (top panel) and the radio monitoring during this period from AMI (see the text). Although there is a significant gap in the AMI coverage owing to earth occultation, preventing a detailed analysis of the radio vs. X-ray behavior, the overlapping coverage is sufficient to demonstrate the onset of radio activity coincident with the strong flaring phase seen by *NuSTAR*.

possibilities in isolation), as noted previously it is quite possible that both of these quantities evolve. Indeed, if we repeat the time-resolved analysis of flare 4 presented in Section 4.4, forcing this to be the case, linking the two with a simple linear relation and assuming that both evolve simultaneously just for illustration ($[h/r_{\rm H}] = 2[r_{\rm in}/r_{\rm ISCO}]$), we again find the same qualitative evolution seen in Figure 15, and the fits are as good as the scenarios in which only one of $r_{\rm in}$ and h is allowed to vary. In this scenario, the magnitude of the changes in $r_{\rm in}$ and h are both reduced in comparison to the decoupled scenarios discussed in Section 4.4, with $r_{\rm in}$ evolving from 1–5 $r_{\rm ISCO}$, and h evolving from 2–10 $r_{\rm H}$. We note that, should the ejecta have reached a significant outflow velocity, the reflection fraction would be reduced for a given combination of h and $r_{\rm in}$ (e.g., Beloborodov 1999) resulting in these quantities potentially being overestimated during the times after the flare, but again the same qualitative evolution should be seen. Furthermore, acceleration up to significant outflow velocities may not be expected so close to the black hole (see Section 5.1.2).

In a flare associated with transient jet ejection, obviously if the jet is the source of illumination, then one naturally expects the height of the source to increase across the flare. However, such ejection events may also be associated with an evacuation of the inner disk, as the same instability that results in the ejection also results in catastrophic accretion of the innermost portion of the disk (Szuszkiewicz & Miller 1998; Meier 2001). Chen et al. (1995) suggest that thin disk solutions should become unstable above luminosities of $\sim$0.3 $L_{\rm E}$, similar to the peak disk fluxes inferred here. Evidence for such behavior might be seen, for example, in GRS 1915+105, where radio ejections are also preceded by dips in X-ray intensity in some of the oscillatory states exhibited by this source, during which the inner radius of the accretion disk is inferred to increase (e.g., Pooley & Fender 1997; Mirabel et al. 1998; Klein-Wolt et al. 2002), though Rodriguez et al. (2008) suggest that the ejections might actually be associated with the post-dip flares observed in those cycles. Similar behavior may also have been seen in the radio galaxies 3C 120 (Marscher et al. 2002; Chatterjee et al. 2009; Lohfink et al. 2013), and 3C 111 (Chatterjee et al. 2011), where radio ejections appear to be preceeded by X-ray dips. Therefore, both an increasing source height and a truncation of the inner accretion disk may be expected for transient ejection events, consistent with the evolution seen in our analysis.

5.1.1. Radio Monitoring

A natural prediction of the jet scenario is that radio emission should be observed. Throughout this recent outburst, V404 Cyg was frequently monitored by the Arcminute Microkelvin Imager–Large Array (hereafter AMI; Zwart et al. 2008), a compact array of eight dishes operating in the 13-18 GHz frequency range. The full AMI campaign on V404 Cyg will be presented in R. Fender et al. (2017, in preparation; see also Mooley et al. 2015); here we focus on the coverage that is simultaneous with our *NuSTAR* observation. Flagging and calibration of the data were performed with the AMI REDUCE software (Perrott et al. 2013). The calibrated data were then imported into CASA and flux densities of V404 Cyg were extracted by vector averaging over all baselines; the absolute flux calibration uncertainty is $\sim$5%.

A comparison of the *NuSTAR* and AMI light curves is shown in Figure 16. Unfortunately, owing to occultation by the Earth, the majority of the flaring period observed by *NuSTAR* does not have simultaneous AMI coverage which, in combination with the frequent Earth-occultations experienced by *NuSTAR*, prevents any detailed analysis attempting to search for radio responses to specific X-ray flares. However, there is AMI coverage right at the beginning of this period, and toward the end of the *NuSTAR* observation. These short periods of overlap do clearly show that radio activity commences as the flaring phase of the *NuSTAR* observation begins, which then appears to persist throughout. The coincidence of this radio activity further supports our suggestion that the major flares seen by *NuSTAR* represent jet ejection events.

5.1.2. Transient Jet Launching

One of the most popular theoretical mechanisms for launching jets is that they are powered by the spin of the central black hole (Blandford & Znajek 1977). The accreting black hole system also may power a Blandford–Payne-type jet (Blandford & Payne 1982) powered instead by the rotation of the accretion disk. It has been suggested that there is observational evidence for a correlation between black hole spin and jet power (taking the peak radio flux as a proxy for jet power) for the transient jet ejections seen from other BHBs at high luminosities (Narayan & McClintock 2012; Steiner et al. 2013), as expected for the Blandford & Znajek (1977) mechanism. However, this is still rather controversial (Russell et al. 2013).

If we are correct and these flares do represent jet ejections in which the jet is the source of illumination for the disk, then our reflection analysis suggests that these jets are launched from very close to the black hole (as close as a few $r_{\rm G}$). The size-scales inferred here are broadly comparable to the size-scale

inferred for the base of the jet in M87 (Asada & Nakamura 2012; Doeleman et al. 2012; Nakamura & Asada 2013), though this is a low-Eddington system that is likely analogous to the persistent jets seen in the low/hard state of BHBs, rather than the high-Eddington transient ejections potentially observed here. One of the other key results from the M87 system is that the acceleration of the outflowing plasma occurs gradually as the distance from the black hole increases; jets do not seem to be immediately launched with relativistic velocities (Nakamura & Asada 2013). This is an important point because it means that the emission from the regions of the jet close to the black hole is unlikely to be heavily beamed, and can therefore illuminate the disk.

As a further point of interest, Koljonen et al. (2015) present evidence for a relation between the photon index of the high-energy X-ray continuum and the frequency at which the low-energy synchrotron spectrum from the jet breaks from optically thick to optically thin emission for a sample of accreting black holes, consisting of both Galactic BHBs and AGNs. This has been derived primarily from data obtained in the low-Eddington jet regime (including low-Eddington observations of V404 Cyg). However, should these high-Eddington ejections adhere to the same relation, the photon indices of $\Gamma \sim 1.1$ seen during the peak of flare 4 would imply a break frequency of $\sim 10^{16}$ Hz at this time. Unfortunately, independent observational constraints on the jet break are not available for this epoch, owing to the lack of simultaneous radio–UV coverage. Nevertheless, should this be correct, this would be among the highest break frequencies inferred among the sample utilized by Koljonen et al. (2015), and would provide further, albeit indirect evidence that the key jet activity in this case occurs very close to the black hole. Indeed, for the jet model discussed in Markoff et al. (2005), a break frequency of $\sim 10^{16}$ Hz would imply a height for the initial zone of particle acceleration of only a few $r_{\rm G}$ above the base of the jet, which would be consistent with the geometric evolution across this flare inferred from the reflection fits presented here.

While not a proof that these ejections are powered by black hole spin, the size-scales inferred here do at least meet one of the expectations for the Blandford & Znajek (1977) mechanism: that the jets should originate from regions very close to the black hole. In addition, our work suggests that V404 Cyg hosts a rapidly rotating black hole (see below), such that it is likely that there would be significant rotational energy for the jets to tap into. However, we are not able to make any further assessment with regards to the correlations presented by Narayan & McClintock (2012) and Steiner et al. (2013) with these data, because it is highly plausible that the available radio coverage missed the peak flux (Figure 16). The large gap in coverage also means we are not able to reliably estimate the total energy of the radio flare, suggested by Fender et al. (2010) and Russell et al. (2013) as an alternative proxy for jet power. The other major possibility, that the jets are primarily powered by the disk rather than the black hole (Blandford & Payne 1982), is also compatible with our results. In this scenario, the implied size-scales would require that the jets be powered in the very innermost regions of the accretion disk.

5.2. Black Hole Spin

Through our investigation of the inner accretion geometry, we are also able to place constraints on the spin of the black hole in V404 Cyg. Our initial modeling of the flux-resolved spectra provided some indication that the black hole spin is high, owing to the strong disk reflection inferred ($R_{\rm disk} \sim 3$). This requires strong gravitational light bending, which in turn requires a high black hole spin, such that the disk can extend very close to the black hole and subtend a large solid angle as seen by the illuminating X-ray source (Miniutti & Fabian 2004; Dauser et al. 2013). Evidence for strong gravitational light bending has previously been observed in a wide variety of active galactic nuclei (e.g., Zoghbi et al. 2008; Fabian et al. 2012; Parker et al. 2014; Reis et al. 2014; Reynolds et al. 2014b; Chiang et al. 2015; Lanzuisi et al. 2016), but also in other Galactic BHBs (e.g., Rossi et al. 2005; Reis et al. 2013). Furthermore, as noted previously, potential evidence for strong reflection has also been seen during flares seen by the *INTEGRAL* coverage of this outburst from V404 Cyg (Natalucci et al. 2015; Roques et al. 2015).

A high spin is supported by our flux-resolved analysis with a self-consistent lamp-post geometry. There is some complexity in the results obtained for the two scenarios considered with the pure lamp-post reflection model (varying the inner radius of the disk while holding the height of the X-ray source constant, and vice versa; Models 2 and 3, respectively), with similarly good fits obtained with high and more moderate-spin solutions in both cases. However, we obtain a significant improvement in the global fit with the inclusion of a contribution from thermal disk emission at the highest fluxes in addition to the lamp-post component (Model 4); this is our best-fit model for the flux-resolved data. In this case, a high spin is unambiguously preferred: $a^* > 0.82$ (see Figure 9, top panel).

In addition, a high spin is also supported by our flare-resolved analysis, focusing on the peaks of the six most extreme flares observed. While this analysis utilizes much less total exposure than our flux-resolved analysis, it has the advantage of relying on much less averaging of different spectra (see Figure 12). The pure lamp-post model strongly requires a high spin (Model 5), but we again see a significant improvement in the fit with the inclusion of a thermal disk component (Model 6); this is our best-fit model for the flare-resolved data. In this case, we see a strong degeneracy between the black hole spin and the inclination of the inner accretion disk, resulting in high- and moderate-spin solutions again providing similarly good fits. The best-fit inclination, $i_{\rm disk} \sim 52°$, which corresponds to the high-spin solution, is in good agreement with the range inferred for the orbital plane of the binary system, $i_{\rm orb} \sim 50°$–$75°$ (e.g., Shahbaz et al. 1994; Khargharia et al. 2010). If we require the inclination to be in this range (Model 6i), then the spin is again strongly required to be high: $a^* > 0.98$ (see Figure 9, bottom panel). Taking a more conservative 99% confidence level, the spin constraint expands to $a^* > 0.92$. Given the lower degree of time-averaging of different spectral "states" in the data analyzed[16] and the good agreement with the orbital inclination, we consider this to be the most robust spin constraint derived from any of our models.

The quantitative constraints on the black hole spin discussed here are the statistical parameter constraints obtained through

[16] While this does formally still occur to some minor degree, this does not appear to have any significant effect on the results obtained. The periods contributing to the Flare 4 spectrum considered in Section 4.3 and shown in Figure 12 are shaded blue in Figure 14. These are drawn from periods T2–6 shown in Figure 15, during which V404 Cyg does show some spectral variations (T2 is notably different to T3–6). However, if we sum the data just from periods T2–5, where the observed spectra are all very similar, the resulting spectra are practically identical to the Flare 4 spectra from Section 4.3.

our spectral modeling. There are additional systematic errors associated with the assumptions inherent to the models used here that are likely significant but difficult to robustly quantify. One issue common to any attempt to constrain black hole spin is the assumption that the accretion disk truncates quickly at the ISCO, and that no significant emission should be observed from within this radius. Numerical simulations suggest that, for thin disks, this is a reasonable assumption (e.g., Reynolds & Fabian 2008; Shafee et al. 2008), and that any additional uncertainty should be small (approximately a few percent), particularly for rapidly rotating black holes.

For the particular case of V404 Cyg considered here, given the extreme luminosities reached during the flares it is worth considering whether the assumption of a thin disk is reasonable. Standard accretion theory predicts that as the accretion flow becomes more luminous, its scale height should start to increase as vertical support from radiation pressure becomes more prominent (e.g., Shakura & Sunyaev 1973). Indeed, some thickness to the disk may be required in order for the disk to be able to anchor the magnetic fields required for jet ejections (e.g., Meier 2001; Tchekhovskoy & McKinney 2012). This is potentially important for both the issue of how quickly the disk truncates at the ISCO, as thicker disks are more able to exhibit emission that "spills over" the ISCO slightly (e.g., Reynolds & Fabian 2008), and also for the self-consistent lamp-post reflection models, which calculate the expected reflection contribution assuming a thin disk geometry (Dauser et al. 2013; García et al. 2014).

In Section 4.3, we estimated the peak disk luminosities to be $L_{\rm disk} \sim 0.3$–$0.5\ L_{\rm E}$. Typically, the high-energy power-law emission from Galactic BHBs is assumed to arise from Compton up-scattering of disk photons, and so the intrinsic disk luminosities would have to be further corrected for the flux lost into the power-law component (e.g., Steiner et al. 2009). This may well be the case at times outside of the flare peaks. However, as noted above, during the flares the power-law emission is likely too hard to originate via Compton scattering of disk photons. If we are correct about the magnetic/jet ejection nature of these flares, then we should be able to take the peak disk fluxes at roughly face value. Therefore, we take $L_{\rm disk}/L_{\rm E} \lesssim 0.5$. For the calculations of the expected disk structure presented in McClintock et al. (2006), this would correspond to a maximum scale height of $h_{\rm D}/r_{\rm D} \lesssim 0.2$, or equivalently a half-opening angle for the inner disk of $\lesssim 10°$. This is unlikely to be large enough that our assumption of a thin disk would lead to large errors. Even if we are incorrect and the high-energy continuum does arise through up-scattering of disk photons, since photon number (rather than flux) is conserved, the peak intrinsic disk fluxes would only have been $\sim$20% larger, even accounting for the hard X-ray flux bent away from the observer in our strong light-bending scenario. Indeed, Straub et al. (2011) find that the X-ray spectrum of LMC X-3 is still fairly well described by a thin disk model up to luminosities of $L_{\rm disk} \sim 0.6\ L_{\rm E}$. Furthermore, while the flare peaks are extreme, the majority of the good exposure obtained naturally covers lower fluxes, during which the thin disk approximation should be even more reliable in terms of the reflection modeling. We therefore expect that, while there may be some mild deviation from the thin disk approximation during the peaks of the flares that could serve to relax the constraints on the spin slightly, this is unlikely to result in major errors, and our conclusion that V404 Cyg hosts a rapidly rotating black hole is likely robust to such issues.

6. Conclusions

The behavior exhibited by V404 Cyg during its recent 2015 outburst is highly complex. Our *NuSTAR* observation obtained during the height of this outburst activity revealed extreme variability, both in terms of the observed flux and also the spectral properties of V404 Cyg. In part, these variations are driven by strong and variable line-of-sight absorption, as seen in previous outbursts from this source. However, strong flares reaching approximately Eddington in the *NuSTAR* bandpass are also observed, during which the central source appears to be relatively unobscured. These flares instead show clear evidence for a strong contribution from relativistic reflection, providing a means to probe the geometry of the innermost accretion flow. We argue that these flares represent transient jet ejection events, during which the ejected plasma is the source of illumination for the accretion disk. This is based on the combination of their observed properties, analogy with other Galactic BHBs, and also the simultaneous onset of radio activity with the period of intense X-ray flaring observed. If we are correct, then our modeling of the relativistic reflection with a lamp-post approximation implies that these jets are launched in very close proximity to the black hole (within a few $r_{\rm G}$), consistent with expectations for jet launching models that tap either the spin of the central black hole, or rotation of the very innermost accretion disk. In addition, our analysis allows us to place constraints on the black hole spin. Although there are some quantitative differences between the different models constructed, we consider our most robust spin constraint to be $a^* > 0.92$ (99% statistical uncertainty only). To the best of our knowledge, this is the first spin constraint for V404 Cyg.

The authors thank the anonymous reviewer for suggestions that helped to improve the manuscript. D.J.W., P.G., and M.J.M. acknowledge support from STFC Ernest Rutherford fellowships (grant ST/J003697/2). K.P.M. acknowledges support from the Hintze Foundation. A.L.K. acknowledges support from NASA through an Einstein Postdoctoral Fellowship (grant number PF4-150125) awarded by the *Chandra* X-ray Center, operated by the Smithsonian Astrophysical Observatory for NASA under contract NAS8-03060. A.C.F. acknowledges support from ERC Advanced Grant 340442. L.N. wishes to acknowledge the Italian Space Agency (ASI) for Financial support by ASI/INAF grant I/037/12/0-011/13. This research has made use of data obtained with *NuSTAR*, a project led by Caltech, funded by NASA and managed by NASA/JPL, and has utilized the NUSTARDAS software package, jointly developed by the ASDC (Italy) and Caltech (USA). This research has also made use of data from AMI, which is supported by the ERC, and we thank the AMI staff for scheduling these radio observations.

Facilities: *NuSTAR*, AMI.

Appendix
A. Lower Spin Solutions

As discussed in the main text, for a number of the models presented in Sections 4.2 and 4.3, we find the $\Delta\chi^2$ curves for the black hole spin to show two similarly good solutions. Specifically, this is the case for our flux-resolved analysis prior

Table 6
Results for the Lower-spin Solutions for Models 2 and 3 (Flux-resolved Analysis)

Model Component	Parameter		Global	Flux Level				
				F1	F2	F3	F4	F5
Model 2: truncating disk, static corona								
RELXILLLP	Γ	...	...	$1.42^{+0.01}_{-0.05}$	$1.44^{+0.01}_{-0.02}$	1.40 ± 0.01	$1.37^{+0.01}_{-0.02}$	1.37 ± 0.01
	$E_{\rm cut}$	(keV)	...	>620[a]	330 ± 60	190 ± 10	126^{+8}_{-6}	92^{+4}_{-2}
	a^*	...	$0.82^{+0.02}_{-0.07}$	...	...	...	...	...
	i	(°)	34 ± 1	...	...	...	...	...
	h	($r_{\rm H}$)	<2.1	...	...	...	...	...
	$A_{\rm Fe}$	(solar)	3.0 ± 0.1	...	...	...	...	...
	$r_{\rm in}$	($r_{\rm ISCO}$)	...	1.7 ± 0.2	1.5 ± 0.1	1.3 ± 0.1	<1.2	1 (fixed)
	$R_{\rm disk}$[b]	...	...	1.1	1.4	1.5	1.7	2.0
	Norm	...	...	0.51 ± 0.05	$0.64^{+0.25}_{-0.06}$	$0.88^{+0.12}_{-0.04}$	$1.27^{+0.44}_{-0.09}$	$2.15^{+0.06}_{-0.08}$
χ^2/DoF			10657/10313					
Model 3: stable disk, dynamic corona								
RELXILLLP	Γ	...	...	$1.38^{+0.05}_{-0.03}$	$1.43^{+0.02}_{-0.01}$	$1.39^{+0.02}_{-0.01}$	1.37 ± 0.01	1.38 ± 0.01
	$E_{\rm cut}$	(keV)	...	>510	320^{+30}_{-40}	190 ± 10	126^{+5}_{-7}	94 ± 3
	a^*	...	$0.64^{+0.05}_{-0.03}$	...	...	...	...	...
	i	(°)	31 ± 1	...	...	...	...	...
	h	($r_{\rm H}$)	...	$2.9^{+1.8}_{-0.4}$	$2.8^{+0.6}_{-0.3}$	2.3 ± 0.2	<2.1	<2.2
	$A_{\rm Fe}$	(solar)	$2.95^{+0.05}_{-0.06}$	...	...	...	...	...
	$R_{\rm disk}$[b]	...	...	1.5	1.5	1.6	1.6	1.6
	Norm	...	...	$0.23^{+0.07}_{-0.04}$	$0.32^{+0.04}_{-0.08}$	$0.57^{+0.13}_{-0.02}$	$1.08^{+0.10}_{-0.12}$	$1.85^{+0.14}_{-0.35}$
χ^2/DoF			10674/10313					

Notes.
[a] $E_{\rm cut}$ is constrained to be $\leqslant$1000 keV following García et al. (2015).
[b] For these models, $R_{\rm disk}$ is calculated self-consistently in the lamp-post geometry from a^*, h, and $r_{\rm in}$. Because it is not a free parameter, errors are not estimated.

Table 7
Results for the Lower-spin Solution for Models 6 (Flare-resolved Analysis)

Model Component	Parameter		Global	Flare					
				1	2	3	4	5	6
Model 6: lamp-post with disk emission									
TBABS$_{\rm src}$	$N_{\rm H}$	(10^{22} cm^{-2})	...	$0.9^{+0.9}_{-0.6}$	$1.7^{+0.5}_{-0.9}$	<2.3	<1.2	$1.9^{+1.2}_{-1.0}$	2.0 ± 0.7
DISKBB	$T_{\rm in}$	(keV)	$0.50^{+0.08}_{-0.04}$	...	...	...	...	...	...
	Norm	(10^5)	...	<0.3	$1.2^{+1.3}_{-0.7}$	$1.0^{+1.6}_{-0.5}$	$0.7^{+1.0}_{-0.2}$	$1.2^{+1.8}_{-0.7}$	$1.1^{+1.4}_{-0.6}$
RELXILLLP	Γ	...	...	<1.03[b]	$1.29^{+0.04}_{-0.02}$	1.37 ± 0.08	1.37 ± 0.07	$1.17^{+0.05}_{-0.08}$	$1.23^{+0.04}_{-0.05}$
	$E_{\rm cut}$	(keV)	...	40 ± 2	119^{+15}_{-14}	37^{+5}_{-4}	67^{+14}_{-11}	50^{+2}_{-7}	80^{+11}_{-6}
	a^*	...	$0.45^{+0.42}_{-0.25}$	...	...	...	...	...	...
	i	(°)	<20	...	...	...	...	...	...
	h	($r_{\rm H}$)	...	$2.9^{+2.7}_{-0.7}$	$6.2^{+4.0}_{-3.2}$	$11.1^{+21.2}_{-4.2}$	$6.6^{+7.1}_{-2.1}$	$7.6^{+32.6}_{-2.7}$	$11.2^{+19.6}_{-5.8}$
	$\log \xi_{\rm disk}$	log (erg cm s^{-1})	...	3.6 ± 0.1	4.0 ± 0.1	3.7 ± 0.1	3.8 ± 0.1	3.8 ± 0.1	4.0 ± 0.1
	$A_{\rm Fe}$	(solar)	$5.0^{+0.3}_{-0.1}$	...	...	...	...	...	...
	$R_{\rm disk}$[a]	...	...	1.4	1.2	1.1	1.2	1.2	1.1
	Norm	...	...	0.9 ± 0.4	$0.8^{+0.3}_{-0.1}$	0.4 ± 0.1	$0.6^{+0.2}_{-0.1}$	0.6 ± 0.1	$0.6^{+0.2}_{-0.1}$
XSTAR$_{\rm abs}$	$\log \xi$	log (erg cm s^{-1})	$5.0^{+0.4}_{-0.3}$	...	...	...	...	...	...
	$N_{\rm H}$	(10^{21} cm^{-2})	...	29^{+12}_{-7}	<3	<10	<10	<9	<6
XILLVER	Norm	...	...	$0.20^{+0.04}_{-0.05}$	$0.26^{+0.10}_{-0.05}$	0.13 ± 0.07	$0.23^{+0.08}_{-0.09}$	0.33 ± 0.06	$0.33^{+0.08}_{-0.04}$
χ^2/DoF			5906/5852						

Notes.
[a] For these models, $R_{\rm disk}$ is calculated self-consistently in the lamp-post geometry from a^* and h. As it is not a free parameter, errors are not estimated.
[b] The RELXILLLP model is only calculated for $\Gamma \geqslant 1$.

to the inclusion of an accretion disk component (Models 2 and 3, Section 4.2), and our flare-resolved analysis when the disk component is included (Model 6, Section 4.3). Based on our flare-resolved analysis, which minimizes the effects of averaging over different spectral forms, we favor the high-spin case, because it is the solution that gives the best agreement between the inferred disk inclination and the known orbital inclination. We therefore present the results for the high-spin solutions for these models in the main manuscript. However, for completeness, here we present the parameter constraints for the lower of the two spin solutions found for Models 2, 3, and 6 (Tables 6 and 7). As stated in the text, where these solutions are not the global best fit, the errors are calculated as $\Delta\chi^2 = 2.71$ around the local minimum.

References

Arnaud, K. A. 1996, in ASP Conf. Ser.101, Astronomical Data Analysis Software and Systems V, ed. G. H. Jacoby & J. Barnes (San Francisco, CA: ASP), 17
Asada, K., & Nakamura, M. 2012, ApJL, 745, L28
Bachetti, M., Harrison, F. A., Cook, R., et al. 2015, ApJ, 800, 109
Beardmore, A. P., Willingale, R., Kuulkers, E., et al. 2016, MNRAS, 462, 1847
Belloni, T. M., & Motta, S. E. 2016, arXiv:1603.07872
Beloborodov, A. M. 1999, ApJL, 510, L123
Bernardini, F., & Cackett, E. M. 2014, MNRAS, 439, 2771
Blandford, R. D., & Payne, D. G. 1982, MNRAS, 199, 883
Blandford, R. D., & Znajek, R. L. 1977, MNRAS, 179, 433
Brenneman, L. W., Reynolds, C. S., Nowak, M. A., et al. 2011, ApJ, 736, 103
Brightman, M., Baloković, M., Stern, D., et al. 2015, ApJ, 805, 41
Casares, J., Charles, P. A., & Naylor, T. 1992, Natur, 355, 614
Chatterjee, R., Marscher, A. P., Jorstad, S. G., et al. 2009, ApJ, 704, 1689
Chatterjee, R., Marscher, A. P., Jorstad, S. G., et al. 2011, ApJ, 734, 43
Chen, X., Abramowicz, M. A., Lasota, J.-P., Narayan, R., & Yi, I. 1995, ApJL, 443, L61
Chiang, C.-Y., Walton, D. J., Fabian, A. C., Wilkins, D. R., & Gallo, L. C. 2015, MNRAS, 446, 759
Corbel, S., Fender, R. P., Tomsick, J. A., Tzioumis, A. K., & Tingay, S. 2004, ApJ, 617, 1272
Corbel, S., Fender, R. P., Tzioumis, A. K., et al. 2002, Sci, 298, 196
Corbel, S., Kaaret, P., Fender, R. P., et al. 2005, ApJ, 632, 504
Corral-Santana, J. M., Casares, J., Muñoz-Darias, T., et al. 2016, A&A, 587, A61
Dauser, T., García, J., Parker, M. L., Fabian, A. C., & Wilms, J. 2014, MNRAS, 444, L100
Dauser, T., García, J., Walton, D. J., et al. 2016, A&A, 590, A76
Dauser, T., García, J., Wilms, J., et al. 2013, MNRAS, 430, 1694
Dauser, T., Wilms, J., Reynolds, C. S., & Brenneman, L. W. 2010, MNRAS, 409, 1534
Dexter, J., McKinney, J. C., Markoff, S., & Tchekhovskoy, A. 2014, MNRAS, 440, 2185
Doeleman, S. S., Fish, V. L., Schenck, D. E., et al. 2012, Sci, 338, 355
Done, C., Gierliński, M., & Kubota, A. 2007, ARv, 15, 1
El-Batal, A. M., Miller, J. M., Reynolds, M. T., et al. 2016, ApJL, 826, L12
Fabian, A. C., Done, C., & Ghisellini, G. 1988, MNRAS, 232, 21P
Fabian, A. C., Lohfink, A., Kara, E., et al. 2015, MNRAS, 451, 4375
Fabian, A. C., Parker, M. L., Wilkins, D. R., et al. 2014, MNRAS, 439, 2307
Fabian, A. C., Rees, M. J., Stella, L., & White, N. E. 1989, MNRAS, 238, 729
Fabian, A. C., Zoghbi, A., Wilkins, D., et al. 2012, MNRAS, 419, 116
Fender, R., & Gallo, E. 2014, SSRv, 183, 323
Fender, R. P., Belloni, T. M., & Gallo, E. 2004, MNRAS, 355, 1105
Fender, R. P., Gallo, E., & Russell, D. 2010, MNRAS, 406, 1425
Fragos, T., Tremmel, M., Rantsiou, E., & Belczynski, K. 2010, ApJL, 719, L79
Fuerst, F., Grinberg, V., Tomsick, J. A., et al. 2016, arXiv:1604.08644
Fürst, F., Müller, C., Madsen, K. K., et al. 2016, ApJ, 819, 150
Fürst, F., Nowak, M. A., Tomsick, J. A., et al. 2015, ApJ, 808, 122
Gandhi, P., Littlefair, S. P., Hardy, L. K., et al. 2016, MNRAS, 459, 554
García, J., Dauser, T., Lohfink, A., et al. 2014, ApJ, 782, 76
García, J., & Kallman, T. R. 2010, ApJ, 718, 695
García, J. A., Dauser, T., Steiner, J. F., et al. 2015, ApJL, 808, L37
Gierliński, M., & Done, C. 2004, MNRAS, 349, L7
González-Hernández, J. I., Casares, J., Rebolo, R., et al. 2011, ApJ, 738, 95
Grefenstette, B. W., Glesener, L., Krucker, S., et al. 2016, ApJ, 826, 20
Haardt, F., & Maraschi, L. 1993, ApJ, 413, 507
Harrison, F. A., Craig, W. W., Christensen, F. E., et al. 2013, ApJ, 770, 103
Heinz, S., Corrales, L., Smith, R., et al. 2016, ApJ, 825, 15
Homan, J., Neilsen, J., Allen, J. L., et al. 2016, ApJ, 830, 5
Jenke, P. A., Wilson-Hodge, C. A., Homan, J., et al. 2016, arXiv:1601.00911
Kaaret, P., Corbel, S., Tomsick, J. A., et al. 2003, ApJ, 582, 945
Kallman, T., & Bautista, M. 2001, ApJS, 133, 221
Kara, E., Zoghbi, A., Marinucci, A., et al. 2015, MNRAS, 446, 737
Khargharia, J., Froning, C. S., & Robinson, E. L. 2010, ApJ, 716, 1105
Kimura, M., Isogai, K., Kato, T., et al. 2016, Natur, 529, 54
King, A. L., Miller, J. M., Bietenholz, M., et al. 2016, NatPh, 12, 772
King, A. L., Miller, J. M., Raymond, J., Reynolds, M. T., & Morningstar, W. 2015, ApJL, 813, L37
Kitamoto, S., Tsunemi, H., Miyamoto, S., Yamashita, K., & Mizobuchi, S. 1989, Natur, 342, 518
Klein-Wolt, M., Fender, R. P., Pooley, G. G., et al. 2002, MNRAS, 331, 745
Koljonen, K. I. I., Russell, D. M., Fernández-Ontiveros, J. A., et al. 2015, ApJ, 814, 139
Kuulkers, E., & Ferrigno, C. 2016, ATel, 8512
Lanzuisi, G., Perna, M., Comastri, A., et al. 2016, A&A, 590, A77
Laor, A. 1991, ApJ, 376, 90
Lasota, J.-P. 2001, NewAR, 45, 449
Lohfink, A. M., Reynolds, C. S., Jorstad, S. G., et al. 2013, ApJ, 772, 83
Madsen, K. K., Harrison, F. A., Markwardt, C. B., et al. 2015a, ApJS, 220, 8
Madsen, K. K., Reynolds, S., Harrison, F., et al. 2015b, ApJ, 801, 66
Markoff, S., Nowak, M. A., & Wilms, J. 2005, ApJ, 635, 1203
Marscher, A. P., Jorstad, S. G., Gómez, J.-L., et al. 2002, Natur, 417, 625
McClintock, J. E., Remillard, R. A., Rupen, M. P., et al. 2009, ApJ, 698, 1398
McClintock, J. E., Shafee, R., Narayan, R., et al. 2006, ApJ, 652, 518
Meier, D. L. 2001, ApJL, 548, L9
Merloni, A., & Fabian, A. C. 2001, MNRAS, 321, 549
Middleton, M. 2015, arXiv:1507.06153
Middleton, M. J., Miller-Jones, J. C. A., Markoff, S., et al. 2013, Natur, 493, 187
Middleton, M. J., Sutton, A. D., Roberts, T. P., Jackson, F. E., & Done, C. 2012, MNRAS, 420, 2969
Miller, J. M., Parker, M. L., Fuerst, F., et al. 2013, ApJL, 775, L45
Miller, J. M., Pooley, G. G., Fabian, A. C., et al. 2012, ApJ, 757, 11
Miller, J. M., Raymond, J., Fabian, A., et al. 2006, Natur, 441, 953
Miller, J. M., Reynolds, C. S., Fabian, A. C., Miniutti, G., & Gallo, L. C. 2009, ApJ, 697, 900
Miller, J. M., Tomsick, J. A., Bachetti, M., et al. 2015, ApJL, 799, L6
Miller-Jones, J. C. A., Jonker, P. G., Dhawan, V., et al. 2009, ApJL, 706, L230
Miniutti, G., & Fabian, A. C. 2004, MNRAS, 349, 1435
Mirabel, I. F., Dhawan, V., Chaty, S., et al. 1998, A&A, 330, L9
Mitsuda, K., Inoue, H., Koyama, K., et al. 1984, PASJ, 36, 741
Mooley, K., Fender, R., Anderson, G., et al. 2015, ATel, 7658
Motta, S. E., Kajava, J. J. E., Sánchez-Fernández, C., Giustini, M., & Kuulkers, E. 2016, arXiv:1607.02255
Muñoz-Darias, T., Casares, J., Mata Sánchez, D., et al. 2016, Natur, 534, 75
Nakamura, M., & Asada, K. 2013, ApJ, 775, 118
Narayan, R., & McClintock, J. E. 2012, MNRAS, 419, L69
Natalucci, L., Fiocchi, M., Bazzano, A., et al. 2015, ApJL, 813, L21
Nealon, R., Price, D. J., & Nixon, C. J. 2015, MNRAS, 448, 1526
Neilsen, J., & Lee, J. C. 2009, Natur, 458, 481
Niedźwiecki, A., Zdziarski, A. A., & Szanecki, M. 2016, ApJL, 821, L1
Oosterbroek, T., van der Klis, M., van Paradijs, J., et al. 1997, A&A, 321, 776
Parker, M. L., Tomsick, J. A., Kennea, J. A., et al. 2016, ApJL, 821, L6
Parker, M. L., Wilkins, D. R., Fabian, A. C., et al. 2014, MNRAS, 443, 1723
Perrott, Y. C., Scaife, A. M. M., Green, D. A., et al. 2013, MNRAS, 429, 3330
Ponti, G., Fender, R. P., Begelman, M. C., et al. 2012, MNRAS, 422, L11
Pooley, G. G., & Fender, R. P. 1997, MNRAS, 292, 925
Punsly, B., & Rodriguez, J. 2013, ApJ, 764, 173
Punsly, B., Rodriguez, J., & Trushkin, S. A. 2016, ApJ, 826, 5
Radhika, D., Nandi, A., Agrawal, V. K., & Mandal, S. 2016, MNRAS, 462, 1834
Rahoui, F., Coriat, M., & Lee, J. C. 2014, MNRAS, 442, 1610
Rahoui, F., Tomsick, J. A., Gandhi, P., et al. 2017, MNRAS, 465, 4468
Rana, V., Loh, A., Corbel, S., et al. 2016, ApJ, 821, 103
Reis, R. C., Fabian, A. C., & Miller, J. M. 2010, MNRAS, 402, 836
Reis, R. C., Fabian, A. C., Ross, R. R., & Miller, J. M. 2009, MNRAS, 395, 1257
Reis, R. C., Miller, J. M., Reynolds, M. T., et al. 2013, ApJ, 763, 48
Reis, R. C., Reynolds, M. T., Miller, J. M., & Walton, D. J. 2014, Natur, 507, 207

Remillard, R. A., & McClintock, J. E. 2006, ARA&A, 44, 49
Reynolds, C. S. 2014, SSRv, 183, 277
Reynolds, C. S., & Fabian, A. C. 2008, ApJ, 675, 1048
Reynolds, C. S., Lohfink, A. M., Ogle, P. M., et al. 2015, ApJ, 808, 154
Reynolds, M. T., & Miller, J. M. 2013, ApJ, 769, 16
Reynolds, M. T., Reis, R. C., Miller, J. M., Cackett, E. M., & Degenaar, N. 2014a, MNRAS, 441, 3656
Reynolds, M. T., Walton, D. J., Miller, J. M., & Reis, R. C. 2014b, ApJL, 792, L19
Risaliti, G., Harrison, F. A., Madsen, K. K., et al. 2013, Natur, 494, 449
Rivers, E., Risaliti, G., Walton, D. J., et al. 2015, ApJ, 804, 107
Rodriguez, J., Cadolle Bel, M., Alfonso-Garzón, J., et al. 2015, A&A, 581, L9
Rodriguez, J., Hannikainen, D. C., Shaw, S. E., et al. 2008, ApJ, 675, 1436
Roques, J.-P., Jourdain, E., Bazzano, A., et al. 2015, ApJL, 813, L22
Ross, R. R., & Fabian, A. C. 2005, MNRAS, 358, 211
Rossi, S., Homan, J., Miller, J. M., & Belloni, T. 2005, MNRAS, 360, 763
Russell, D. M., Gallo, E., & Fender, R. P. 2013, MNRAS, 431, 405
Sanchez-Fernandez, C., Kajava, J. J. E., Motta, S. E., & Kuulkers, E. 2016, arXiv:1608.08802
Sanwal, D., Robinson, E. L., Zhang, E., et al. 1996, ApJ, 460, 437
Shafee, R., McKinney, J. C., Narayan, R., et al. 2008, ApJL, 687, L25
Shahbaz, T., Bandyopadhyay, R., Charles, P. A., & Naylor, T. 1996, MNRAS, 282, 977
Shahbaz, T., Ringwald, F. A., Bunn, J. C., et al. 1994, MNRAS, 271, L10
Shakura, N. I., & Sunyaev, R. A. 1973, A&A, 24, 337
Sivakoff, G. R., Bahramian, A., Altamirano, D., et al. 2015a, ATel, 7959
Sivakoff, G. R., Bahramian, A., Heinke, C. O., et al. 2015b, ATel, 7788
Steiner, J. F., & McClintock, J. E. 2012, ApJ, 745, 136
Steiner, J. F., McClintock, J. E., & Narayan, R. 2013, ApJ, 762, 104
Steiner, J. F., McClintock, J. E., & Reid, M. J. 2012, ApJL, 745, L7
Steiner, J. F., McClintock, J. E., Remillard, R. A., Narayan, R., & Gou, L. 2009, ApJL, 701, L83
Steiner, J. F., Reis, R. C., McClintock, J. E., et al. 2011, MNRAS, 416, 941
Straub, O., Bursa, M., Sądowski, A., et al. 2011, A&A, 533, A67
Straub, O., Done, C., & Middleton, M. 2013, A&A, 553, A61
Szuszkiewicz, E., & Miller, J. C. 1998, MNRAS, 298, 888
Tchekhovskoy, A., & McKinney, J. C. 2012, MNRAS, 423, L55
Terada, K., Miyamoto, S., Kitamoto, S., & Egoshi, W. 1994, PASJ, 46, 677
Tetarenko, B. E., Sivakoff, G. R., Heinke, C. O., & Gladstone, J. C. 2016, ApJS, 222, 15
Tomsick, J. A., Corbel, S., Fender, R., et al. 2003, ApJ, 582, 933
Tomsick, J. A., Nowak, M. A., Parker, M., et al. 2014, ApJ, 780, 78
Vasilopoulos, G., & Petropoulou, M. 2016, MNRAS, 455, 4426
Verner, D. A., Ferland, G. J., Korista, K. T., & Yakovlev, D. G. 1996, ApJ, 465, 487
Wagner, R. M., Kreidl, T. J., Howell, S. B., & Starrfield, S. G. 1992, ApJL, 401, L97
Walton, D., Harrison, F., Forster, K., et al. 2015a, ATel, 7797
Walton, D., Harrison, F., Forster, K., et al. 2015b, ATel, 7752
Walton, D. J., Nardini, E., Fabian, A. C., Gallo, L. C., & Reis, R. C. 2013, MNRAS, 428, 2901
Walton, D. J., Reis, R. C., Cackett, E. M., Fabian, A. C., & Miller, J. M. 2012, MNRAS, 422, 2510
Walton, D. J., Risaliti, G., Harrison, F. A., et al. 2014, ApJ, 788, 76
Walton, D. J., Tomsick, J. A., Madsen, K. K., et al. 2016, ApJ, 826, 87
Wik, D. R., Hornstrup, A., Molendi, S., et al. 2014, ApJ, 792, 48
Wilkins, D. R., & Fabian, A. C. 2012, MNRAS, 424, 1284
Wilkins, D. R., Gallo, L. C., Grupe, D., et al. 2015, MNRAS, 454, 4440
Wilms, J., Allen, A., & McCray, R. 2000, ApJ, 542, 914
Zdziarski, A. A., Poutanen, J., Paciesas, W. S., & Wen, L. 2002, ApJ, 578, 357
Zoghbi, A., Fabian, A. C., & Gallo, L. C. 2008, MNRAS, 391, 2003
Zwart, J. T. L., Barker, R. W., Biddulph, P., et al. 2008, MNRAS, 391, 1545
Zycki, P. T., Done, C., & Smith, D. A. 1999a, MNRAS, 309, 561
Zycki, P. T., Done, C., & Smith, D. A. 1999b, MNRAS, 305, 231